DTIC FILE COPY

①

NTATION PAGE

Form Approved
OMB No 0704-0188

1a. REPC UNCLASSIFIED		1b RESTRICTIVE MARKINGS NONE			
2a. SECURITY CLASSIFICATION AUTHORITY		3. DISTRIBUTION/AVAILABILITY OF REPORT APPROVED FOR PUBLIC RELEASE; DISTRIBUTION UNLIMITED.			
2b. DECLASSIFICATION/DOWNGRADING SCHEDULE					
4. PERFORMING ORGANIZATION REPORT NUMBER(S)		5. MONITORING ORGANIZATION REPORT NUMBER(S) AFIT/CI/CIA-88-214			
6a. NAME OF PERFORMING ORGANIZATION AFIT STUDENT AT Univ of Oklahoma	6b. OFFICE SYMBOL (If applicable)	7a. NAME OF MONITORING ORGANIZATION AFIT/CIA			
6c. ADDRESS (City, State, and ZIP Code)		7b. ADDRESS (City, State, and ZIP Code) Wright-Patterson AFB OH 45433-6583			
8a. NAME OF FUNDING/SPONSORING ORGANIZATION	8b. OFFICE SYMBOL (If applicable)	9 PROCUREMENT INSTRUMENT IDENTIFICATION NUMBER			
8c. ADDRESS (City, State, and ZIP Code)		10. SOURCE OF FUNDING NUMBERS			
		PROGRAM ELEMENT NO.	PROJECT NO.	TASK NO	WORK UNIT ACCESSION NO

11. TITLE (Include Security Classification) (UNCLASSIFIED)
An investigation into the Gravity Current Aspects of a Cold Air Outbreak Using Variational Analysis Techniques

12. PERSONAL AUTHOR(S)
Stephen Bond Allen

13a. TYPE OF REPORT THESIS/XXXXXXXXXXX	13b. TIME COVERED FROM _____ TO _____	14. DATE OF REPORT (Year, Month, Day) 1988	15. PAGE COUNT 92

16. SUPPLEMENTARY NOTATION APPROVED FOR PUBLIC RELEASE IAW AFR 190-1
ERNEST A. HAYGOOD, 1st Lt, USAF
Executive Officer, Civilian Institution Programs

17.	COSATI CODES		18. SUBJECT TERMS (Continue on reverse if necessary and identify by block number)
FIELD	GROUP	SUB-GROUP	

19. ABSTRACT (Continue on reverse if necessary and identify by block number)

DTIC
ELECTE
JUN 02 1989
S
H
D

▶ 89 6 02 020

20. DISTRIBUTION/AVAILABILITY OF ABSTRACT ☒ UNCLASSIFIED/UNLIMITED ☐ SAME AS RPT ☐ DTIC USERS	21. ABSTRACT SECURITY CLASSIFICATION UNCLASSIFIED	
22a. NAME OF RESPONSIBLE INDIVIDUAL ERNEST A. HAYGOOD, 1st Lt, USAF	22b. TELEPHONE (Include Area Code) (513) 255-2259	22c. OFFICE SYMBOL AFIT/CI

DD Form 1473, JUN 86   Previous editions are obsolete   SECURITY CLASSIFICATION OF THIS PAGE

AFIT CI "OVERPRINT"

THE UNIVERSITY OF OKLAHOMA

GRADUATE COLLEGE

AN INVESTIGATION INTO THE GRAVITY CURRENT

ASPECTS OF A COLD AIR OUTBREAK

USING VARIATIONAL ANALYSIS TECHNIQUES

A THESIS

SUBMITTED TO THE GRADUATE FACULTY

in partial fulfillment of the requirements for the

degree of

MASTER of SCIENCE

in METEOROLOGY

By

STEPHEN BOND ALLEN

Norman, Oklahoma

1988

AN INVESTIGATION INTO THE GRAVITY CURRENT

ASPECTS OF A COLD AIR OUTBREAK

USING VARIATIONAL ANALYSIS

TECHNIQUES

A THESIS

APPROVED FOR THE SCHOOL OF METEOROLOGY

By

Acknowledgments

I give my heartfelt thanks to Dr. Yoshi Sasaki for his kind and thought provoking advice. His vision, direction and encouragement were an immense help in this investigation. I thank Dr. Glen Lesins and Dr. Kelvin Droegemeier for their advice and constructive criticism. I thank Dr. L.P.Chiang for his helpful discussions and support and Debbie Hagrman for her help with the data.

TABLE OF CONTENTS

LIST OF TABLES

LIST OF ILLUSTRATIONS

v

LIST OF ILLUSTRATIONS (continued)

ABSTRACT

An Investigation Into the Gravity Current Aspects of a Cold Air Outbreak Using Variational Analysis Techniques.

During the time period of January 27th through January 28th, 1986, the Central and Southeastern U.S. experienced a cold air outbreak. Surface temperatures dropped 30 degrees Fahrenheit in a matter of hours in Central Florida with dramatic drops in dewpoint as well. A method is developed using variational calculus to decompose observed gridded radiosonde data from this period into component fields. Three variational filters are used iteratively to extract the desired components of the observed data. These components are then used in concert with quasi-geostrophic theory to examine the similarities between this cold air outbreak, the gust front associated with an active thunderstorm, and a gravity current. Sensitivity studies of this method with respect to weight factors are shown. Results indicate some of the interactions between synoptic and sub-synoptic forcing in the development and maintenance of such a system.

AN INVESTIGATION INTO THE GRAVITY CURRENT
ASPECTS OF A COLD AIR OUTBREAK
USING VARIATIONAL ANALYSIS TECHNIQUES

CHAPTER I

INTRODUCTION

The formation of atmospheric fronts has been studied extensively over the last twenty years and those associated with the cold air outbreak, hereafter called CAO, have been of special interest. The CAO is common in the Central and Eastern US in winter and is typified by a large accumulation of cold air in Southern Canada that sweeps southeastward. Many times this movement comes in waves as one front forms and moves out to be followed by others in succession.

In order to understand these fronts better one must not only understand the forces responsible for the development of the fronts but also the balance which develops between the frontogenetic and the frontolytic forces. This balance allows the front to be sustained at some quasi-steady intensity over extended periods of time. Williams and Plotkin (1968) showed that much can be learned from the quasi-geostrophic equations of

1

motion. These approximations are not valid for fronts that already exist, however, where the gradients are strong and the Rossby number is close to unity as in the case of the CAO studied here. Hoskins and Bretherton (1972) used the assumption of geostrophic balance only in the cross-front direction, the semi-geostrophic assumption, to show that a balance could be maintained between the frontogenetic process and frictional dissipation. This results in a more realistic front; however, the lack of some method of limiting the production of vorticity due the stretching of the vortex tubes by the divergence field can allow the vorticity to go to infinity. Orlanski and Ross (1984), hereafter called OR, showed that the primitive equations of motion do allow a feedback mechanism between the divergence field and the ageostrophic vorticity field. The equations listed below are the divergence and vorticity equations derived from primitive equations as used by OR.

$$\frac{dD}{dt} = \zeta_a -D^2 -2\alpha^2 +2\alpha D +F_d$$

$$\frac{d\zeta}{dt} = -D(f+\zeta) -\beta v$$

In this form ζ is the relative vorticity, ζ_a is the ageostrophic relative vorticity, D is the divergence, α is the geostrophic background deformation, F_d is the frictional term, f is the Coriolis parameter and $\beta = df/dy$. OR hypothesized that as the front becomes stronger the

ζ_a term starts to dominate the right hand side of the divergence equation, thus effectively controlling the rate of change of the divergence, and subsequently, the frontogenetic process itself. An inspection of this relationship reveals that when the ζ_a is in phase with the divergence field at the front, as in Fig 1a, the convergence at the front will grow. This is a frontogenetic process.

FRONTOGENETIC   STEADY STATE

ζ_a

Div

$\pi/2$
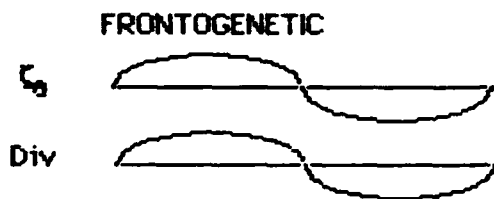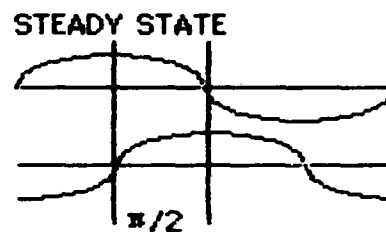
Fig 1a   Fig 1b

If the divergence leads the ζ_a field by some phase shift value, however, this frontogentic effect will diminish until the effect is reversed and the ζ_a will become a negative feedback on the divergence field. Thus we see that factors that can influence the strength or location of the divergence and the ζ_a with respect to the front will be important in controlling the frontogentic process and therefore be important in forming the balance between the frontogenetic and frontolytic forces required for the front to persist.

The importance of the ageostrophic components in this process required the use of a method for obtaining

the most accurate estimate of the ageostrophic components possible. This requirement led to the use of a variational method developed by Sasaki (1958) which calculates a realistic geostrophic state by allowing both the height field and the wind field to adjust but constrains that state to be as close to the observed state as possible in a least square sense. The resultant ageostrophic fields can then be examined in the light of the relationships stated above. In the process of examining these fields it was found that there were numerous similarities between the CAO and a smaller scale feature, the gravity or density current as exhibited by the gust front from an active thunderstorm. These gravity currents are associated with strong areas of convergence at the leading edge, but are basically irrotational in the horizontal plane. Therefore it is speculated that the interaction of the gravity current effects, such as local convergence at the leading edge, with the synoptic effects, such as the background deformation and vorticity, may to some extent control the longevity and intensity of the CAO by helping to produce a phase shift between the divergence and the vorticity fields. OR speculated that gravity wave effects may be responsible for this phase shift.

In order to examine this hypothesis it is necessary to point out the similarities observed between the CAO and a gravity current. This is done by using information about gravity currents obtained through theoretical

studies such as that by Benjamin (1968) and tank
experiments such as that by Simpson (1972) and also by
relating the features of the CAO to gust front cases that
have been related to gravity currents such as the report
by Charba (1974) and the simulations done by Mitchell
and Hovermale (1977) of gust fronts. Some of these
similarities are found in the observed fields; however,
the CAO is a synoptic scale feature and thus the
rotation of the earth can not be ignored as it is
commonly in mesoscale features such as gust fronts.
This difference in scales seems to be at least partially
accounted for in this type of analysis by the fact that
the effects of the rotating earth are largely exhibited in
the geostrophic balance of the heights and winds.
Therefore, it seems plausible that effects observed in
gravity currents or gust fronts which are not on a scale
large enough to exhibit the influence of the rotating
earth should appear in the ageostrophic components of
a synoptic scale feature such as the CAO.

Figs 2a-c are reprinted from Charba (1974) and
depict some of the major features of a thunderstorm
gust front. These features serve as a basis for
comparisons between the CAO and the gust front and
are listed as follows.
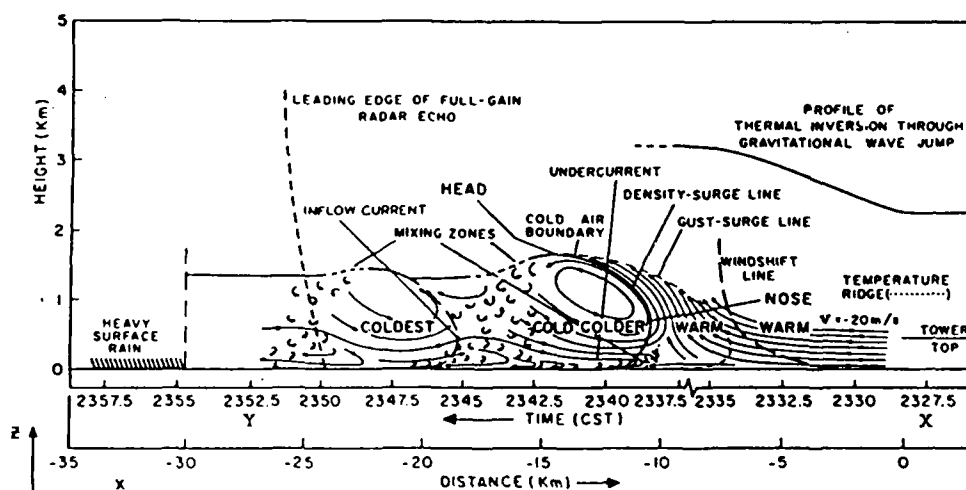
1. Fig 2a shows a pressure trace that increases as
the front passes with one or more pressure jumps
followed by a dip and a pressure or density surge. The
final pressure levels off at some value higher than the
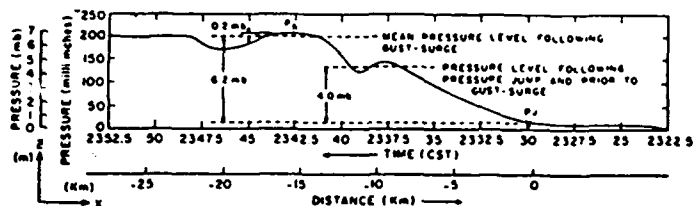
Fig 2a   Pressure tendency
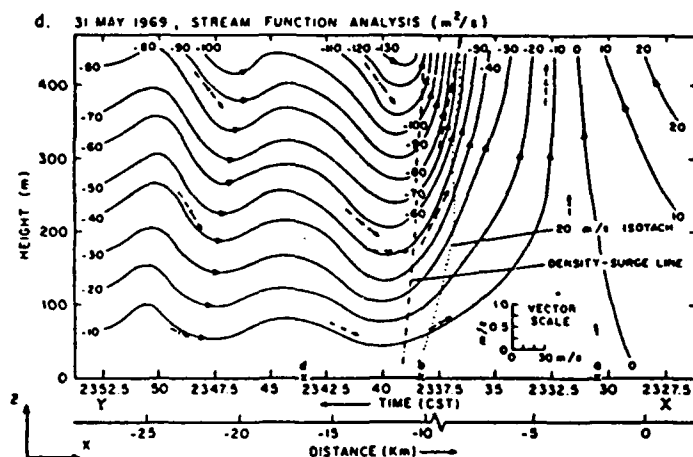
Fig 2b   Stream function analysis

Fig 2c   Gust front cross-section

Fig 2a-c   Gust front features reprinted from Charba (1974)

original pressure.

The remaining features are depicted in Fig 2c.

2. There is a windshift line in the winds parallel to the front (along-front) which preceeds the front by some amount. Just behind this is a minimum in the winds perpendicular to the front (cross-front). The maximum in the cross-front winds occurs somewhat behind the front.

3. There is a thermal ridge located just before the front. This warm area is also indicated in reports from Mitchell and Hovermale (1977), Clarke (1961), Martin (1973), and Shapiro (1984).

4. The shape of the leading edge is curved and may extend forward past the surface position. This protrusion of the front is called the nose.

5. There is an elevated region just behind the front called the head. A roll current is evident in the upper region of the head just behind the front.

6. Behind the head is an area of considerable turbulence and mixing especially in the upper levels.

7. Further behind the head is the tail whose upper extent is somewhat lower than that of the head.

In the descriptions above, the term behind the front indicates a position to the left of the front in these figures. It should also be noted that the horizontal cross-front extent of the gust front depicted here is about 30 km. The propagation speed of this front was about 20 m/s with cross front winds behind the front

of about 25 m/s. The propagation speed of gravity currents and gust fronts vary significantly due to the different surface frict' n encountered, the relative depth of the cold air with respect to the total depth of the fluid or atmosphere, and the density difference between the two fluid or air masses. The propagation speed U of a density current is on the order of tens of m/s and is given by the equation

$$U^2 = k(\Delta\rho/\rho)gH \quad \text{(Daly and Pracht,1968)}$$

where k is the internal Froude number, $\Delta\rho$ is the density difference, ρ is the density of the lighter fluid, g is the gravity and H is the height of the heavier fluid. For gravity currents k is around 1, (Daly and Pracht,1968) and around .5 for larger scale density surges as shown by Berson (1958). These values are found through scale analysis or empirically set so there is some variability. The ratio of the maximum wind speed behind the front to the frontal speed is given experimentally by Simpson (1969) as 1.3. This value is validated by observational results by Charba (1974) and model results by Mitchell and Hovermale (1977).

It is then the intention of this paper to illustrate these features of a gust front/gravity current as they are exhibited in the CAO, to explore the possibility of these features having a controlling effect on the frontogenetical process as it occurs in the frontal zone of the CAO, and to examine the interactions of these effects with the synoptic forces present.

CHAPTER II

SYNOPTIC OVERVIEW

Figs 3-5 show time series of three surface and 500 mb charts which depict the movement and development of several very intense cold fronts over the Southeastern U.S. during the time period of 00z Jan 27, 1986 through 00z Jan 28, 1986. This corresponds to a strong upper level trough which moves slowly across the Eastern U.S. and a strong surface high pressure system which travels south from Northern Canada to Southern Texas during this period. With the passage of these fronts there are dramatic temperature drops of over 30 degrees F in 12 hours in Northern Florida and equally dramatic drops in dewpoints. Different types of cold fronts can also be differentiated during this time period. The cold front present at 00z Jan 27 was typified by weak temperature gradients and strong wind shifts. The cold front that entered Florida at 12z Jan 27th was marked by very little wind shift and very strong temperature gradients. This seems to be associated with a strong cold air outflow typified by the southward migration of the surface high. It is this front that will be studied in depth in this report. Figs 7-9 are

9
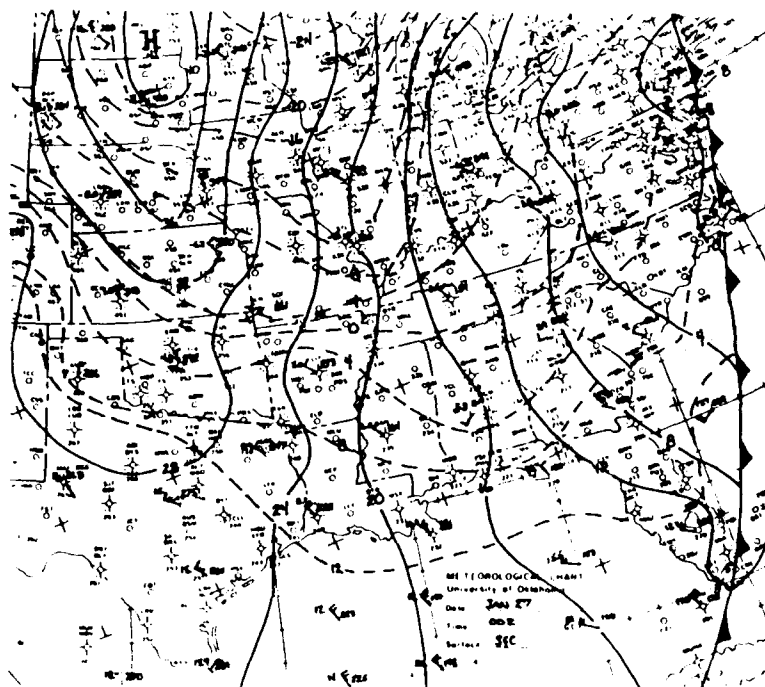
Fig 3a Surface analysis 00z Jan 27,1986
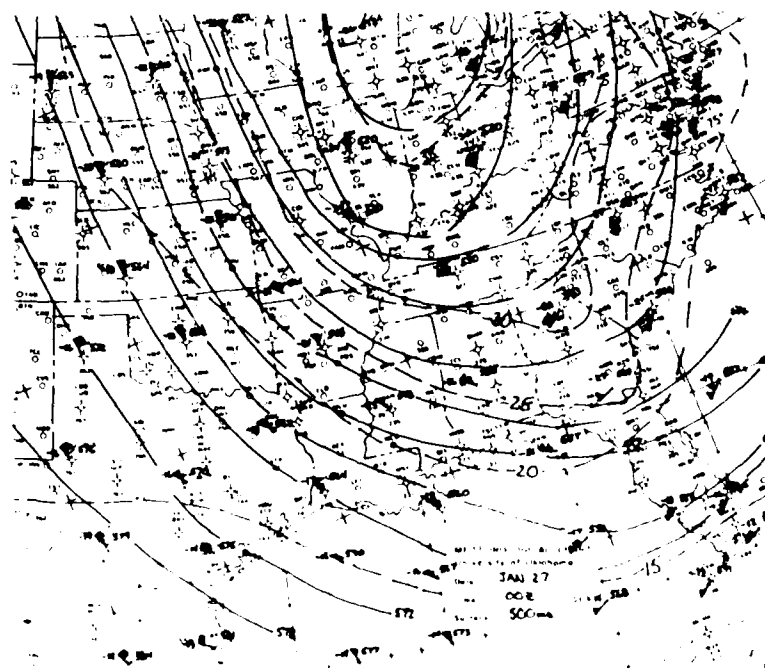
Fig 3b 500 mb analysis 00z Jan 27,1986
Fig 3a-b Isotherms are dashed lines, height contours are
solid lines

Fig 4a   Surface analysis 12z Jan 27,1986

Fig 4b 500 mb analysis 12z Jan 27,1986
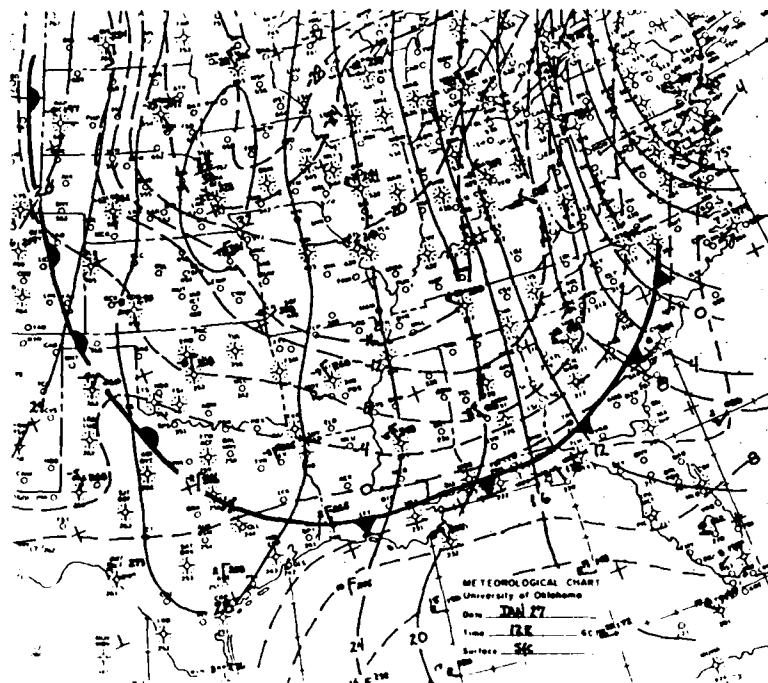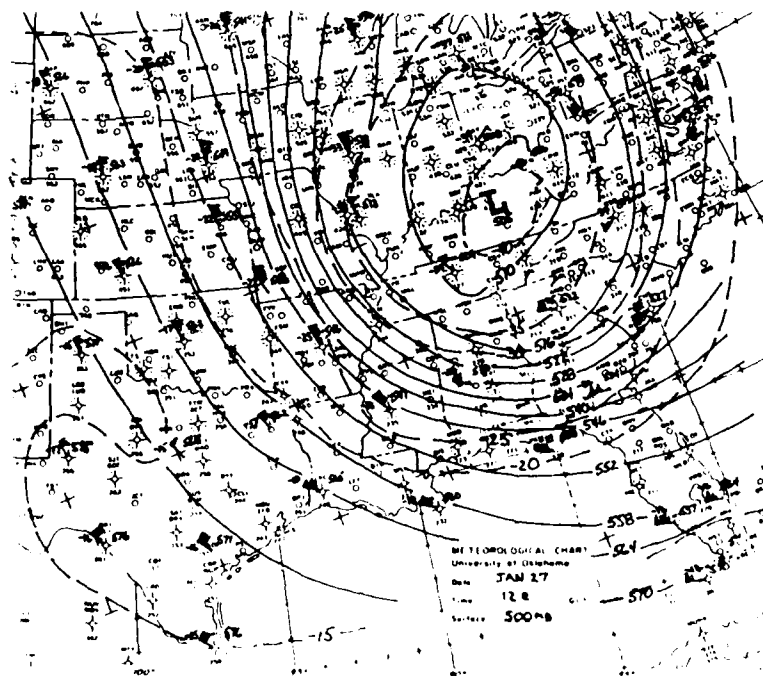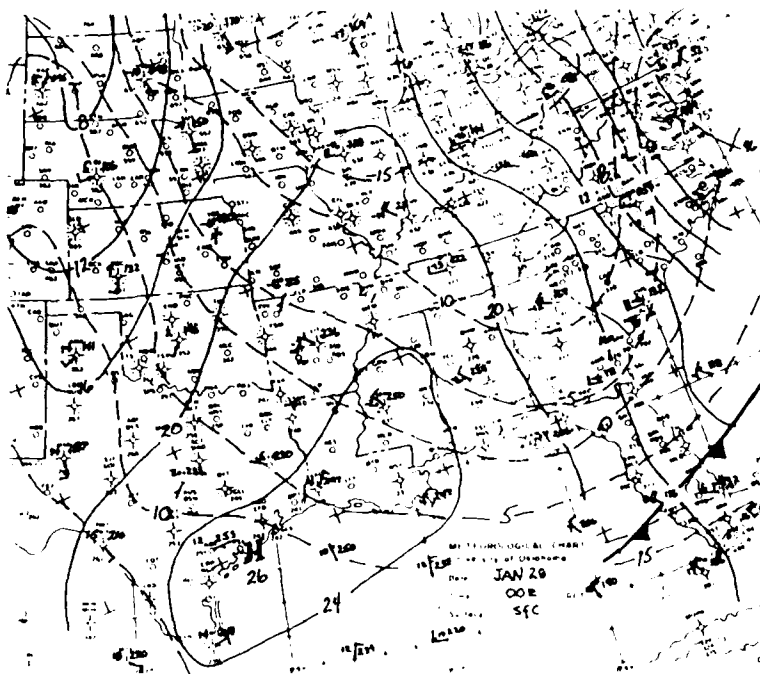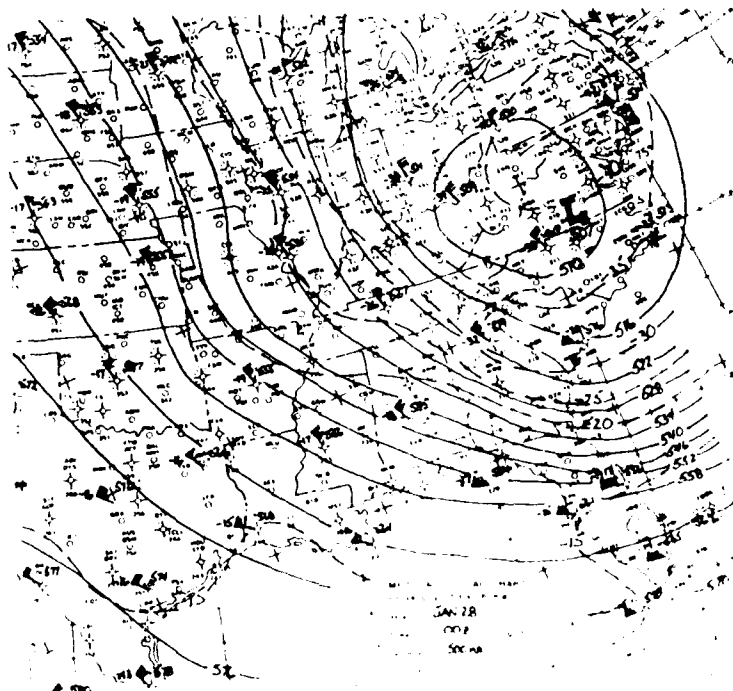**Fig 4a-b   Isotherms are dashed lines, height contours are solid lines**

Fig 5a   Surface analysis 00z Jan 28,1986

Fig 5b 500 mb analysis 00z Jan 28,1986
Fig 5a-b   Isotherms are dashed lines, height contours are solid lines

the plots of potential temperature (θ) at 850, 700, and 500 mb respectively for 00z Jan 27, 1986, hereafter called 00z27, 12 z Jan 27, 1986, hereafter called 12z27, and 00z Jan 28, 1986, hereafter called 00z28. These plots show a very strong temperature gradient has formed by the second time period. Behind this front a cold pool develops that has its center over the southern tip of Illinios. Over this time period, using Central Kentucky as a reference point, θ at 850 mb drops from 273K to 257K. This is a drop of 16K in 24 hours. At 700 mb θ drops from 278K to 273K in 24 hours, a drop of 5K. Thus the stability of the area has increased. This is due in part to radiational cooling which is strongest at the surface. A significant line of strong gradient of θ is also created during this time period which runs north and south from Minnesota to Alabama. An important feature of this system is the slope of the ridge-trough axis. Fig 6 depicts how a ridge-trough system that slopes westward with height is associated with an area of minimum thickness in the height field. Starting from the hydrostatic equation it can be shown that decreasing

FORMATION OF COLD POOL THROUGH WESTWARD SLOPING RIDGE-TROUGH AXIS
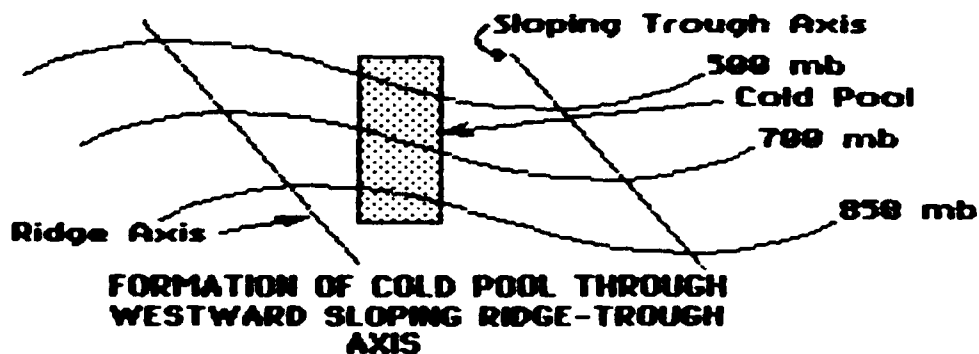
Fig 6
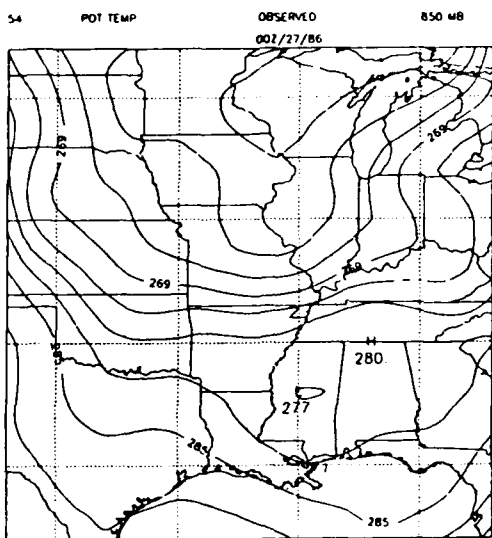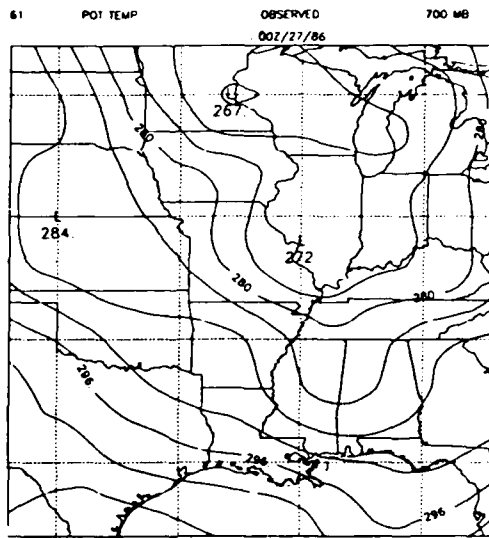
Fig 7a   850 mb

Fig 7b   700 mb
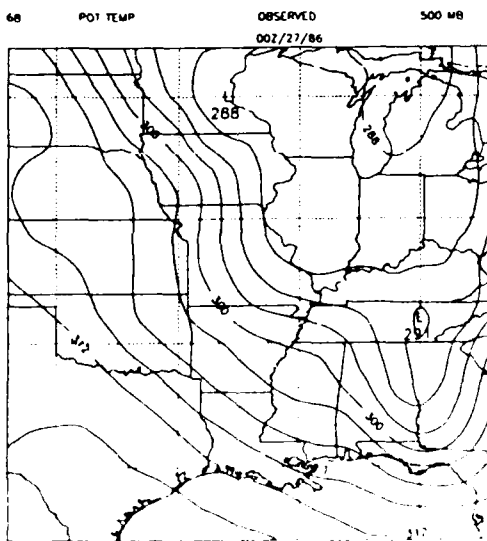
Fig 7c   500 mb

Fig 7a-c   Potential temperature in Kelvin for 00z Jan 27,1986
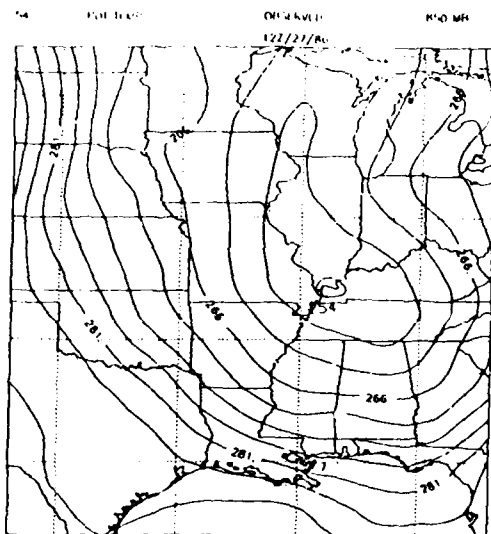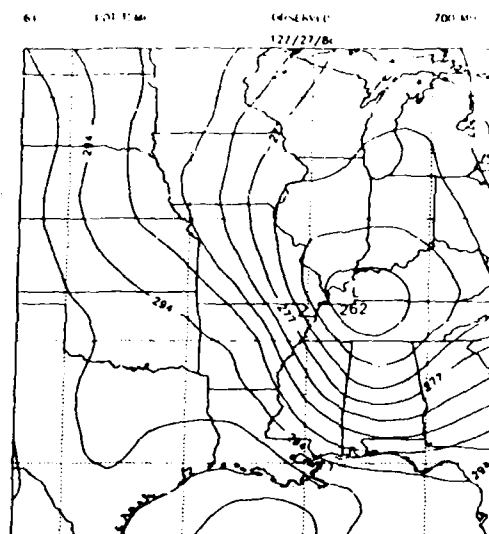
Fig 8a   850 mb   Fig 8b   700 mb
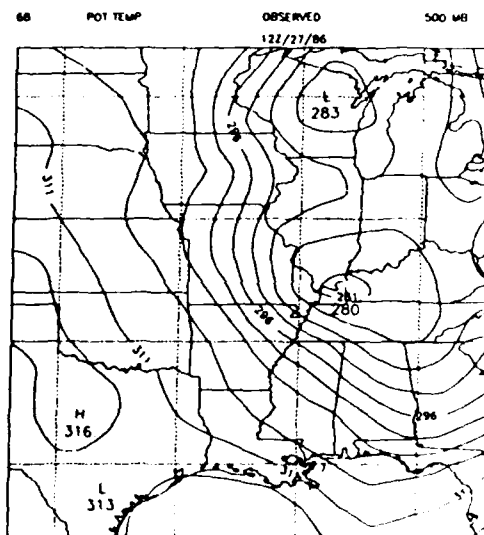
Fig 8c   500 mb

Fig 8a-c   Potential temperature in Kelvin for 12z Jan 27,1986
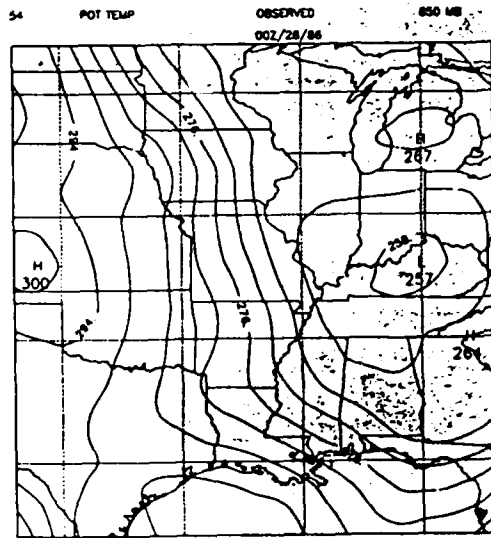
Fig 9a   850 mb
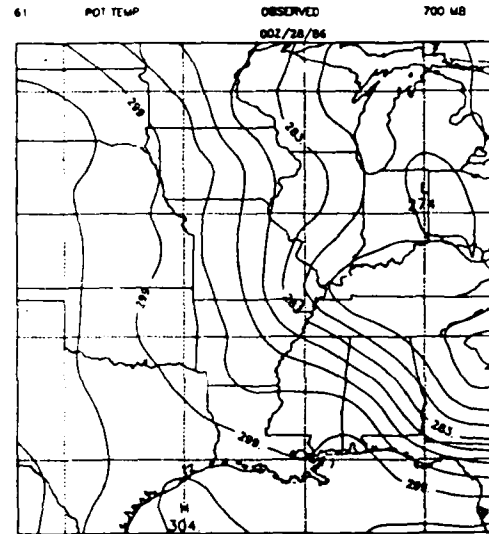
Fig 9b   700 mb
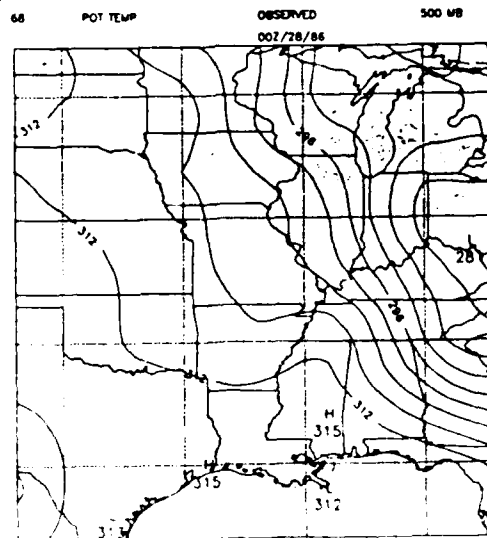
Fig 9c   500 mb

Fig 9a-c Potential temperature in Kelvin for 00z Jan 28,1986

thickness implies decreasing temperature.

$$T=-(1/R)d\phi/d\ln p \quad \text{where } \Theta=T(p_\theta/p)^{R/cp}$$

Thus for a constant -dp (going up) a decrease in dφ means a decrease in Θ. Figs 3-5 indicate the height pattern does indeed slope to the west with height. Figs 10a-c show the geostrophic thickness of the layer from 850 mb to 500 mb for the 24 hour period. Using these values in the above equation one cancalculate the change in thickness over Central Kentucky as 119m over the 24 hour period. This corresponds to a change in Θ of 8.6K. This is actually a little higher than that experienced at the 700 mb level , although it is only half of the change found at the 850 mb level. This can be explained by the differential advection of temperature with height. At 850 mb the wind are northwesterly causing cold advection. The winds veer with height, however, and at 500 mb the winds are advecting warmer temps. Therefore one would expect a greater negative change in Θ in the lower levels than the upper levels as compared to the average change in the layer as predicted by the hydrostatic equation. It should also be noted that the surface high appears to the west of the coldest air aloft rather than directly beneath it. As the surface high moves southward it stays to the west of the strongest line of Θ change but to the east of the upper level ridge in accord with the sloping ridge-trough mechanism described above. In the last time period we see that upper level ridge-trough
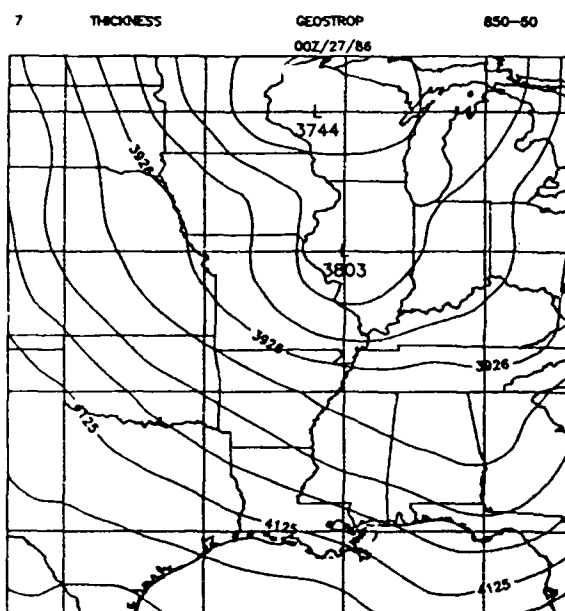
Fig 10a 00z Jan 27,1986
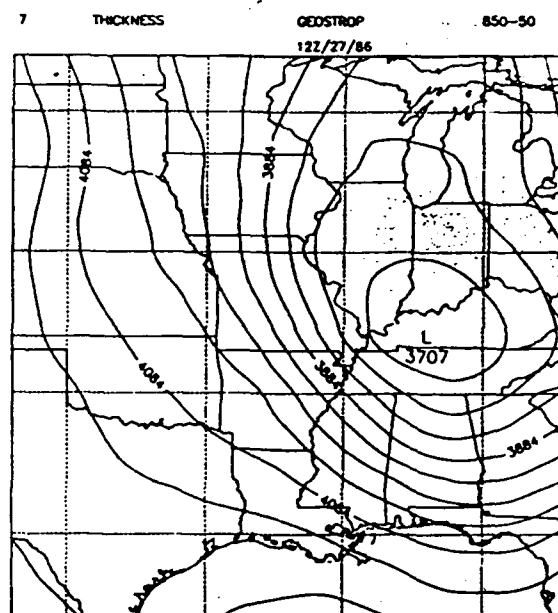
Fig 10b 12z Jan 27,1986
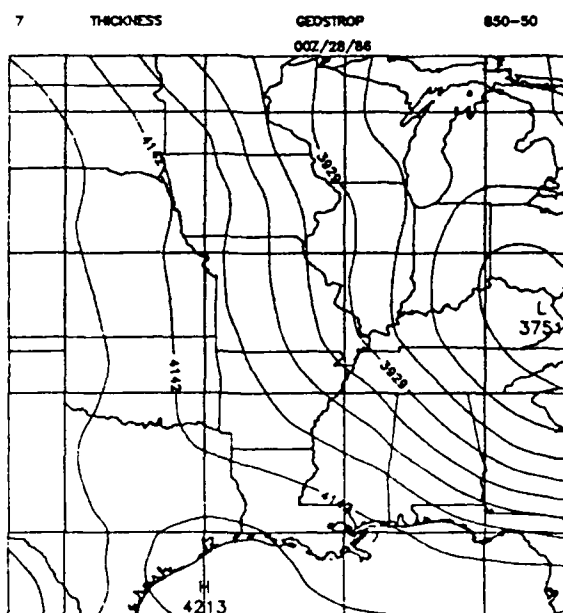
Fig 10c 00z Jan 28,1986

Fig 10a-c Geostrophic thickness of the layer 850 mb to 500 mb in meters.

system has moved eastward and decreased in intensity while the surface high has moved southeastward and decreased in strength. This implies that the effects of the sloping ridge-trough system in enhancing the cold pool are now dissipating and the effects of advection and radiational cooling will become more important.

CHAPTER III

DATA AND OBJECTIVE ANALYSIS

In order to analyze this case a 25x25 degree grid with 1x1 degree grid spacing was used. The grid has its origin in the lower left hand corner at 25 degrees north latitude and 103 degrees west longitude. Upper air data were collected from 66 stations at 5 levels in and around the grid. Reported data were input at 5 levels, those levels being 1000, 850, 700, 500, and 250 mb. Pressure surface heights were input at all 5 levels while winds were input at the top four and temperature and dewpoints were input at the middle three. In data sparse regions, such as over water, data were hand interpolated from NMC charts. Fig 11 shows the grid and the stations used. Stations with reported data are represented as filled circles while interpolated positions are represented as triangles. Additional sounding data were obtained to help verify station data and fill data sparse regions. The raw data were then analyzed onto the grid at the five input levels using a four pass weighted Cressman analysis scheme described in Appendix A. Temperature and height data were then interpolated onto four intermediate levels. The
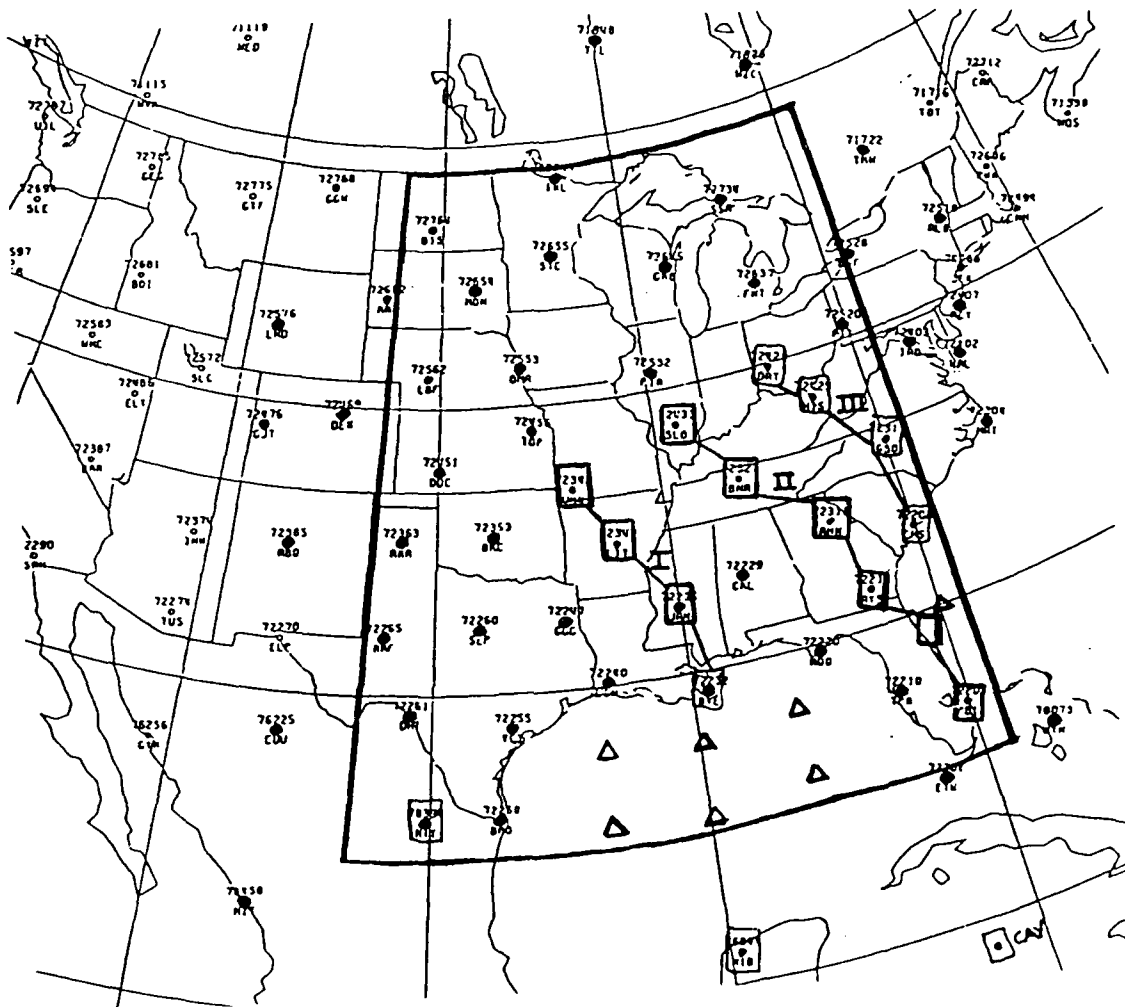
Fig 11 Input station locations and outline of analysis grid. Reporting locations are filled circles, interpolated locations are triangles, squares are additional sounding locations.

intermediate levels were set at the average log pressure
level of the adjacent input levels. These levels are at
972, 771, 592,and 354 mb. Temperatures were
interpolated linearly with the height computed
hydrostatically. These intermediate levels are important
for a smooth fit for the hydrostatic filter. The grid
system is listed by level in Table 1.

TABLE 1

Level	Press mb	Ln(P)	Data present	Filter Used
9	250	398	U,V,PHI	none
8	354	298	T,PHI	H C
7	500	199	U,V,T,TD,PHI	G H C
6	592	151	T,PHI	H C
5	700	102	U,V,T,TD,PHI	G H C
4	771	75	T,PHI	H C
3	850	47	U,V,T,TD,PHI	G H C
2	922	23	T,PHI	H C
1	1000	0	PHI	NONE

U,V	Winds in m/s
T,TD	Temperature and Dewpoint in Kelvin
PHI	Geopotential in m*m/s*s
G	Geostrophic filter
H	Hydrostatic filter
C	Continuity filter

These gridded data were then checked for
consistency against the NMC charts at the input levels
to insure that no errors were present. Two other
methods were used to check for input errors. As the
Cressman analysis proceeds, the gridded data are
interpolated back onto the station locations and the
residuals, the difference between the input value and
the back-interpolated value, are computed and averaged

over the field. These values should decrease with each successive pass. This also is the basis for deciding what radius of influence to use in the analysis. These values were found to be acceptable at all levels. This is explained further in the explanation of the Cressman analysis scheme in Appendix A. Also, since one of the output fields is the difference field between the geostrophic and observed fields, errors in the observed data sometimes appear as large anomolies in the ageostrophic field. These anomolies were checked for validity also.

There has been no smoothing of any of the input data except for that inherent in the Cressman analysis. Also, although data were interpolated into data sparse regions, these regions were usually at the edge of the grid and the resultant fields were always consistent with NMC portrayals and the supplemental soundings obtained. No input station values were changed where reported data was available.

CHAPTER IV

VARIATIONAL METHOD

The method of using variational filters to extract various components of meteorological fields has been used in initialization schemes successfully and is outlined in continuous form in Haltiner and Williams (1980). Appendix A gives the derivation of the finite difference version of the three filters used in this study. There are several points that deserve special attention and each will be mentioned in the description of the filters.
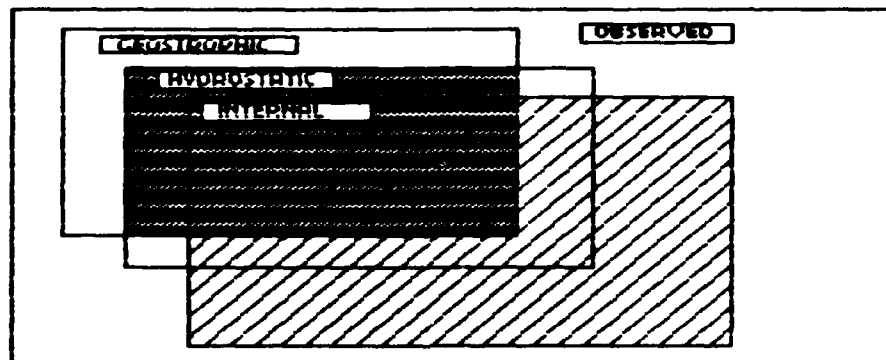
Fig 12

Each of these filters extracts a specific component from the input field. An example of the filtering process is schematically represented in Fig 12. In this depiction the shaded area is the geostrophic-hydrostatic component while the striped area is the

24

internal-ageostrophic component. In order to insure that the final fields are adjusted correctly to all the conditions it is necessary to iterate through the filter sequence shown in Fig 13. Trial and error has shown that three iterations are sufficient for convergence.

VARIATIONAL METHOD
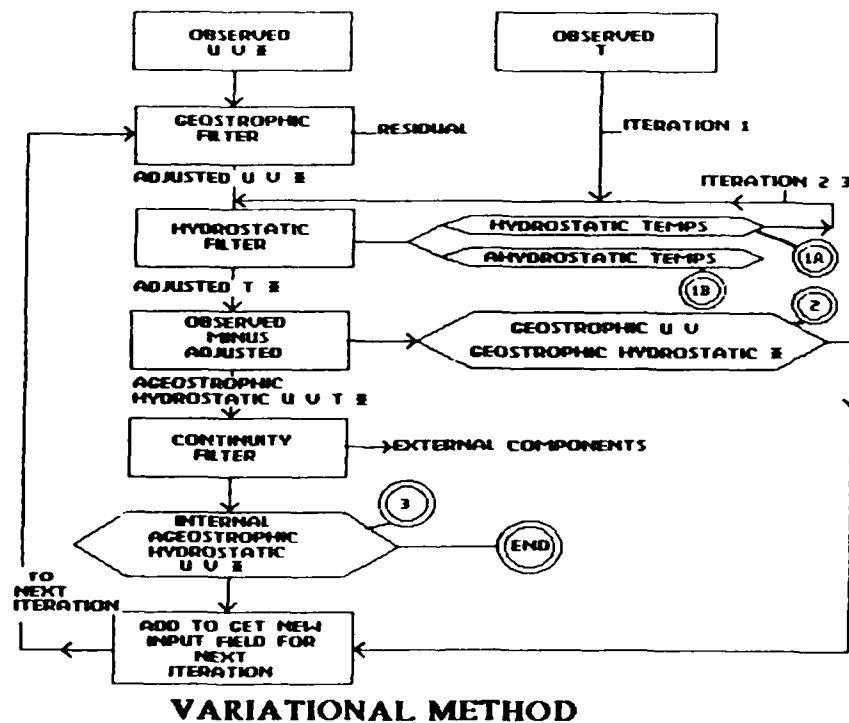
Fig 13

Hydrostatic Filter

The observed height data are computed from the radiosonde temperature and pressure data hydrostatically, but the hydrostatic filter is needed to keep the values in hydrostatic balance during the adjustment process. As stated before, there are height and temperature data at levels 2 through 8 and these are the levels at which the hydrostatic filter adjusts values. The intermediate levels allow for a smoother fit and decrease the error inherent near the boundaries. The adjustment process requires that there be no adjustment at the top and bottom boundaries. Eqn 1 is the finite difference form of the functional for the hydrostatic eqation and Eqns 2-5 are the equations for T and ϕ. The derivations of these equations are listed in appendix A.

EQN 1)

$$J = \Sigma[\alpha(T_{ijk} - To_{ijk})^2 + \beta(\phi_{ijk} - \phi o_{ijk})^2 +$$

$$\lambda_{ijk}(\phi_{ijk+1} - \phi_{ijk-1})/2\Delta P - T_{ijk})]\Delta P$$

where α is the error module for T and β is the error module for ϕ. These error modules are also called precision modules or weight factors. λ is the lagrange multiplier fot the constraint as explained in HW (1980).

EQN 2) $T_{ijk} = \lambda_{ijk}/2\alpha + To_{ijk}$

EQN 3) $\phi_2 = \lambda_3/2\beta\Delta PC + \phi o_2$ For k=2

EQN 4) $\phi_k = (\lambda_{k+1} - \lambda_{k-1})/2\beta\Delta PC + \phi o_k$ For k=3,7

EQN 5) $\phi_8 = -\lambda_7/2\beta\Delta PC + \phi o_8$ For k=8

The appropriate λs are found from the following equations depending on the position in the grid at which

the calculation takes place.

For k=3,7   EQN 7)

$$\lambda_k = \frac{[\lambda_{k+2}/2\beta\Delta PF\Delta PC + \lambda_{k-2}/2\beta\Delta PB\Delta PC + (\phi o_{k+1} - \phi o_{k-1})/\Delta PC - To_k]}{1/2\beta\Delta PF\Delta PC + 1/4\beta\Delta PHB\Delta PC + 1/2\alpha}$$

For k=2   EQN 8)

$$\lambda_k = \frac{[\lambda_{k+2}/2\beta\Delta PF\Delta PC + (\phi o_{k+1} - \phi o_{k-1})/\Delta PC - To_k]}{1/2\beta\Delta PF\Delta PC + 1/4\beta\Delta PHB\Delta PC + 1/2\alpha}$$

For k=8   EQN 9)

$$\lambda_k = \frac{[\lambda_{k-2}/2\beta\Delta PB\Delta PC + (\phi o_{k+1} - \phi o_{k-1})/\Delta PC - To_k]}{1/2\beta\Delta PB\Delta PC + 1/4\beta\Delta PHT\Delta PC + 1/2\alpha}$$

It should be noted that there are several ways to deal with the boundary conditions. In this case it was decided to redefine the finite difference form of the derivatives near the boundaries to forward or backward difference forms with the assumption that λ is zero everywhere on the boundaries and outside the computational domain. The redefined derivatives are indicated in the previous equations by the notation

$$\Delta PC = P_{k+1} - P_{k-1} \quad \Delta PF = P_{k+2} - P_k \quad \Delta PB = P_k - P_{k-2}$$

$$\Delta PHT = P_k - P_{k-1} \quad \Delta PHB = P_{k+1} - P_k$$

where k indicates the pressure level. This method has proven to be acceptable as long as the method is consistent throughout. The "adjusted" field of this filter is the hydrostatic (Hereafter called HYD) component while the residual field of this filter is the non-hydrostatic (Hereafter called AHYD) component.

Geostrophic Filter

Eqns 10 and 11 are the finite difference form of the functionals for the geostrophic adjustment of u and v respectively.

EQN 10)　　$J1 = \sum_i \sum_j [\alpha(u_{ijk} - uo_{ijk})^2 + \beta(\phi_{ijk} - \phi o_{ijk})^2$

$+ \lambda_u (fv + (\phi_{ij+1k} - \phi_{ij-1k})/2\Delta y)] \Delta x \Delta y$

EQN 11)　　$J2 = \sum_i \sum_j [\alpha(v_{ijk} - vo_{ijk})^2 + \beta(\phi_{ijk} - \phi o_{ijk})^2$

$+ \lambda_v (fu + (\phi_{i+1jk} - \phi_{i-1jk})/2\Delta x)] \Delta x \Delta y$

Eqns 12 and 13 are the equations for u and v and have no problems at the boundaries since all computations are made at the gridpoint.

EQN 12)　　　　$u_{ij} = uo_{ij} - (f/2\alpha)\lambda u_{ij}$

EQN 13)　　　　$v_{ij} = vo_{ij} - (f/2\alpha)\lambda v_{ij}$

Eqns 14–18 are the equations for ϕ.

EQN 14)　　$\phi_{i1} = +(1/4\beta\Delta y)\lambda u_{i2} + \phi o_{i1}$　for j=1

EQN 15)　　$\phi_{i2} = +(1/4\beta\Delta y)\lambda u_{i3} + \phi o_{i2}$ for j=2

EQN 16)　　$\phi_{ij} = -(1/4\beta\Delta y)(\lambda u_{ij-1} - \lambda u_{ij+1}) + \phi o_{ij}$　for j=3,n-2

EQN 17)　　$\phi_{in-1} = -(1/4\beta\Delta y)\lambda u_{in-2} + \phi o_{in-1}$　for j=n-1

EQN 18)　　$\phi_{in} = -(1/4\beta\Delta y)\lambda u_{in-1} + \phi o_{in}$　for j=n

It should be noted that although equations for ϕ_{i1} and ϕ_{in} are listed, these values are not adjusted and are always equal to the observed values. This is due to the fact that $\lambda=0$ at all points on the lateral boundaries as

well as one gridpoint in from the boundaries.

EQN 20) $\lambda u_{ij} = [2\alpha\beta(2\Delta y)^2][fuo_{ij} + (\lambda u_{ij+2} + \lambda u_{ij-2})/2\beta(2\Delta y)^2$

$+(\phi o_{ij+1} - \phi o_{ij-1})/2\Delta y]/(f^2\beta(2\Delta y)^2 + 2\alpha)$

EQN 21) $\lambda v_{ij} = [2\alpha\beta(2\Delta x)^2][fvo_{ij} + (\lambda v_{i+2j} + \lambda v_{i-2j})/2\beta(2\Delta x)^2$

$+(\phi o_{i+1j} - \phi o_{i-1j})/2\Delta x]/(f^2\beta(2\Delta x)^2 + 2\alpha)$

This is equivalent to a finite difference form of the continuous Euler-Lagrange equations using centered difference forms of the derivatives spanning $2\Delta x$ and $2\Delta y$ instead of Δx and Δy. This appears to be a necessity to preclude computational instability in the adjustment process (Sasaki and McGinley, 1975). The geostrophic filter adjusts the observed wind to the geostrophic state with the constraint that the adjusted winds be close to the observed winds in a least square sense. A unique result of this technique is that the the observed heights are adjusted at the same time yielding a geostrophic height field that is also close to the observed height field in a least square sense. This type of dual adjustment would appear to be more realistic than computing geostrophic winds from observed heights and although the latter method may be sufficiently accurate for some treatments it is not accurate enough to yield the finer scale information we need for this type of analysis. The geostrophic filter is executed at the 850, 700, and 500 mb levels independently except for the further filtering by the hydrostatic filter which constrains the fields to be hydrostatic.

External Wave Filter

In this study it is desirable to exclude the effects of the high frequency, fast moving, external gravity waves. Therefore, the continuity equation is used to filter the resultant fields excluding most of the external components. This is done via Eqn 22 which is the finite difference form of the continuity equation functional. Eqns 23, 24, and 25 are the equations for u, v, and λ respectively.

EQN 22) $\Sigma_i \Sigma_j \Sigma_k \lambda_k [(u-uo)^2 + (v-vo)^2]\Delta P +$

$\lambda \Sigma ((u_{i+1jk} - u_{i-1jk})/2\Delta x + (v_{ij+1k} - v_{ij-1k})/2\Delta y)\Delta P]\Delta x \Delta y = 0$

EQN 23) $u_i = (\lambda_{i-1} - \lambda_{i+1})/4\Delta x + uo_i$

EQN 24) $v_j = (\lambda_{j-1} - \lambda_{j+1})/4\Delta y + vo_j$

EQN 25) $\lambda_{ij} = [(\lambda_{i+2} + \lambda_{i-2})\Delta y^2 + (\lambda_{j+2} + \lambda_{j-2})\Delta x^2]$

$/2(\Delta x^2 + \Delta y^2) - 2/P_s \Sigma_p [[(uo_{i+1} - uo_{i-1})\Delta y + (vo_{j+1} - vo_{j-1})\Delta x]/(\Delta x^2 + \Delta y^2)]\Delta P$

Where P_s is $\Sigma_p \Delta P$

During the adjustment process the residuals of the individual fields should get very small. The residual of a field is defined as the rms average value of that field when operated on by the appropriate constraint equation. Thus in the case of the geostrophic filter, the adjusted u, v, and ϕ were operated upon at all gridpoints by the geostrophic constraint equation and the rms deviation from zero was computed and averaged at each level. For complete accuracy this value should be zero. The error modules α and β for

each filter are recomputed at each iteration and these values should get very large. We can see in Table 2 that the values do follow this pattern. Iteration 4 was tested, but the values changed very little.

Table 2

Iteration			
Geostrophic	1	2	3
u residual	.19E-3	.37E-10	.27E-10
α	.1E+2	.73E+2	.65E+16
β	.18E+14	.1E+17	.1E+17
Hydrostatic			
T residual	.79E-1	0.0	0.0
α	.27E+13	.27E+13	.1E+17
β	.14E+16	.1E+17	.1E+17
External Wave			
residual	1.8603333	1.8603333	1.8603333

Table 2 is only a representative set showing the progress of the adjustment process for all three filters for 00z Jan 27 850 mb.

In order to do the second and third iterations meaningfully it was necessary to add the geostrophic-hydrostatic-internal component (GEO) and the ageostrophic-hydrostatic-internal component (AGEO) together and use this as the input field for the next iteration.

Comparison of the final output fields show very good agreement with the expected results. One thing to note is that since no adjustment will occur on the boundaries, the last two grid points next to the boundaries will carry systematic errors and are not plotted in the output field representations. In the

hydrostatic case the systematic errors are confined to one gridpoint in the vertical. Three separate tests were run to check the sensitivity of the results to the boundary conditions. In the first test random values up to +/- 3 m/s were added to the observed winds on all lateral boundaries. In the second test random values of +/- 10 m were added to the observed height field on all lateral boundaries. In each test observed values were used at all other gridpoints. The AGEO wind, height, and divergence fields were then compared to the original analysis. In the third test random values of +/- 3 degrees C were added to all gridpoints on level 2 and 8. The AHYD field was then compared to the original analysis. In all three test no significant changes were found in the resultant fields. By moving the grid several degrees it was determined that the features shown in the output fields were not grid dependent and showed good consistency of position except for a slight tendency to close off features near the edges of the plots.

The weight factors or error modules α and β in each filter have a definite effect upon the resultant adjustment process. This effect was tested by rerunning the same cases for different values of α and β to see how the resultant fields changed. Figs 14-16 are representative results of these tests and show the expected results. The ratio of one weight factor to the other in each functional controls the relative amount

that value will be adjusted. In the geostrophic filter this means that if α, the weight factor for winds, is very large compared to β, the weight factor for heights, the heights will be adjusted more than the winds. Therefore in Fig 14 as α becomes very large wrt β we see that the GEO wind become very similar to the observed wind (the AGEO winds get lighter). Conversely, when β becomes large, as in Fig 15, compared to α we see that the GEO ϕ field becomes similar to the observed field (the AGEO ϕ get smaller). Fig 16 shows the AHYD temperature field for α large compared to β in the hydrostatic filter. Here again we see that in this case the AHYD temperatures get smaller. The crucial thing to note here is that in all the tests run for different weight factors, the basic pattern remained the same. Where there were highs with one set of weights, there were highs in all other sets. The same held true for lows. Therefore, although the absolute value of output fields can be altered by using different weight factors, the relative shape of the fields is not alterable and is consistent throughout. This result is both expected and absolutely necessary for the results of the filtering process to be meaningful.

Other output fields fall under the categories of derived fields and supplemental fields. Derived fields are computed using output from the filtering process such as the kinematic ω. Supplemental fields are moisture, frontogenesis, etc. The methods for computing these

$\alpha_g = 1.0$
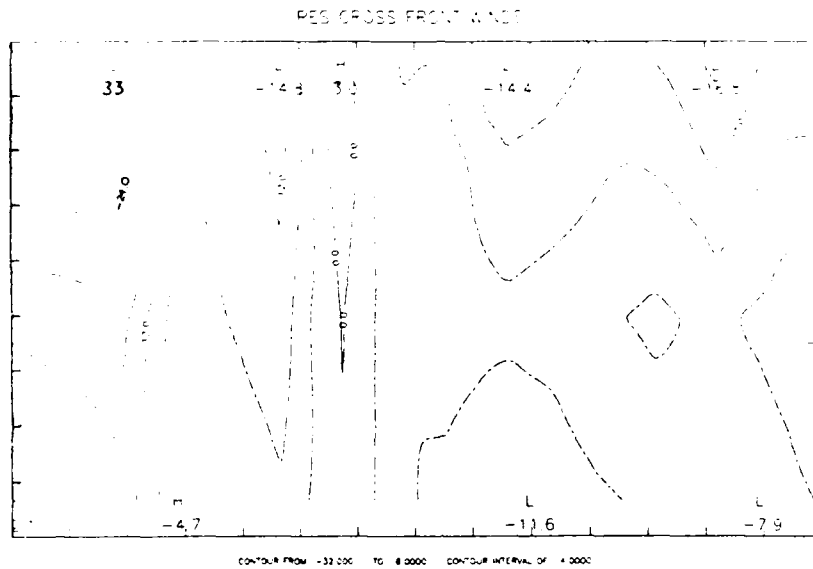
Fig 14a   Height test $\alpha_g = 1.0$
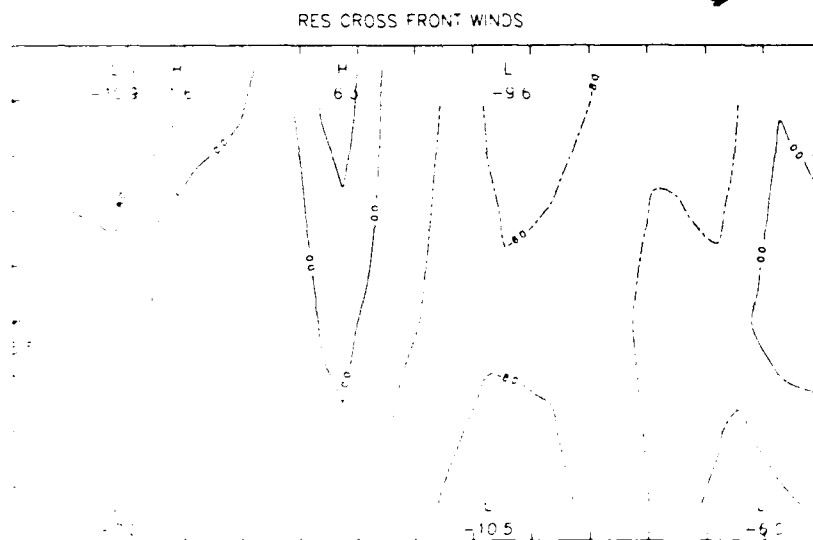
$\alpha_g = 100.0$

Fig 14b   Height test $\alpha_g = 100.0$

Fig 14a-b   Test for geostrophic wind error module α_g. 14a shows ageostrophic winds found with std α_g. 14b shows same with   std $\alpha_g \ast 100$.
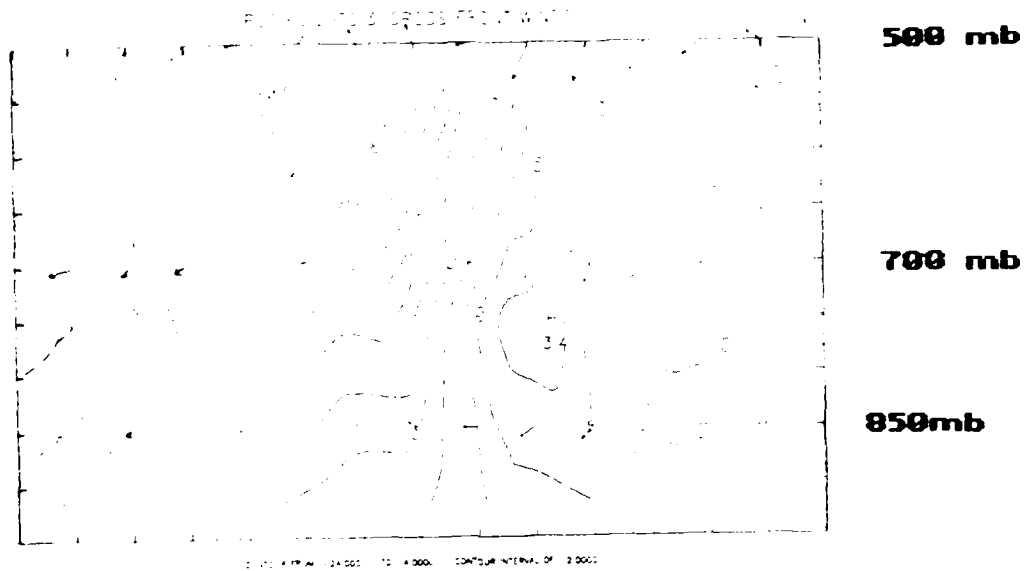
Fig 15a   Weight test β_g=0.01
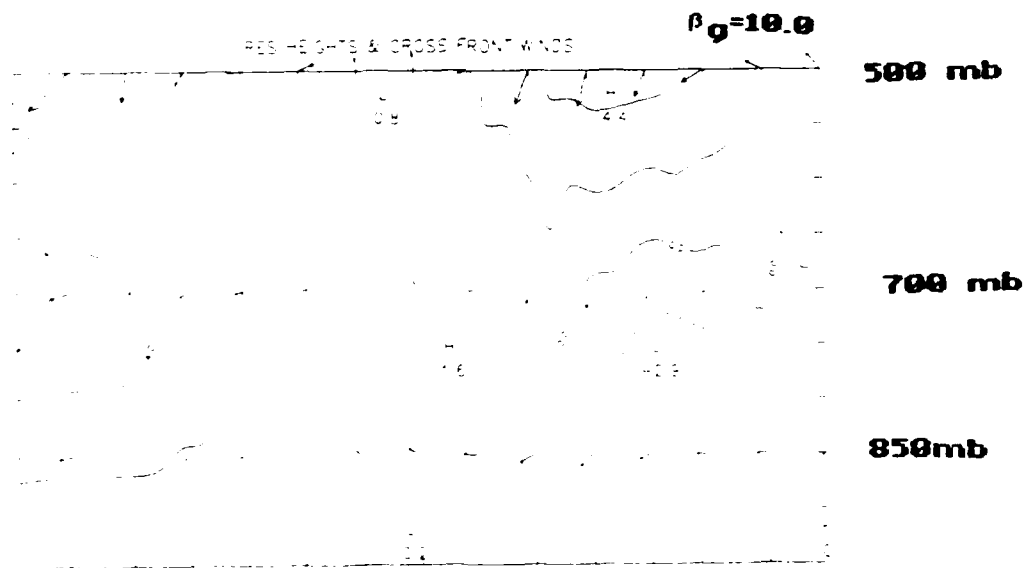
Fig 15b   Weight test β_g=10.0

Fig 15a-b   Test for geostrophic height error module β_g.
15a shows ageostrophic heights found with std β_g. 15b
shows same with   std β_g*1000

$\alpha_h = 50.0$

RES TEMPERATURE

500 mb

700 mb

850mb

CONTOUR FROM -3.0000 TO 3.0000 CONTOUR INTERVAL OF 1.0000

Fig 16a   Height test α_h=50.

$\alpha_h = 5000.0$

RES TEMPERATURE

500 mb

700 mb

850mb

A

CONTOUR FROM -3.0000 TO 3.0000 CONTOUR INTERVAL OF 1.0000

B
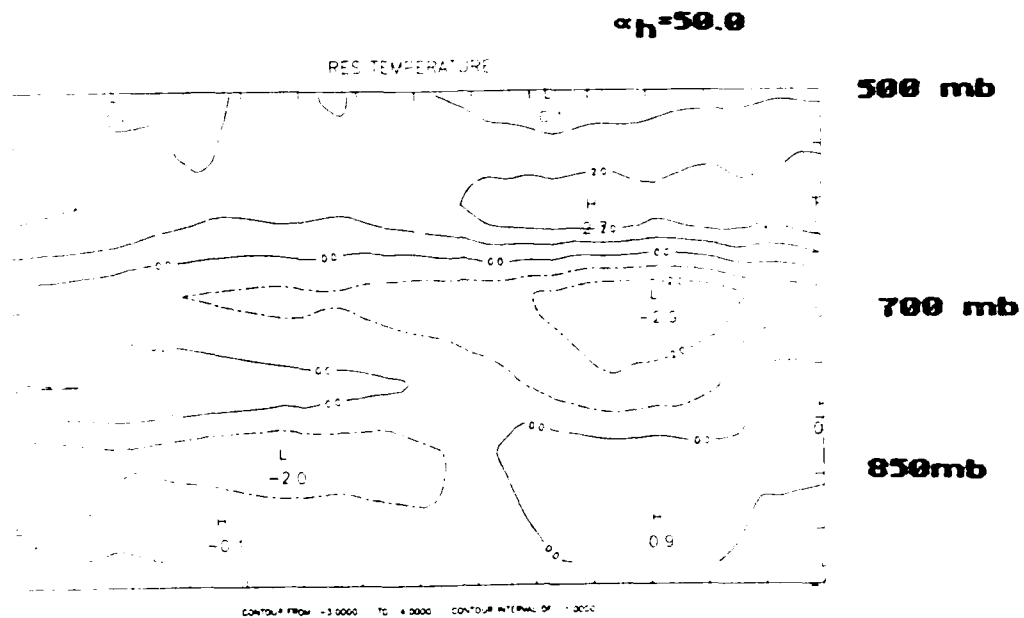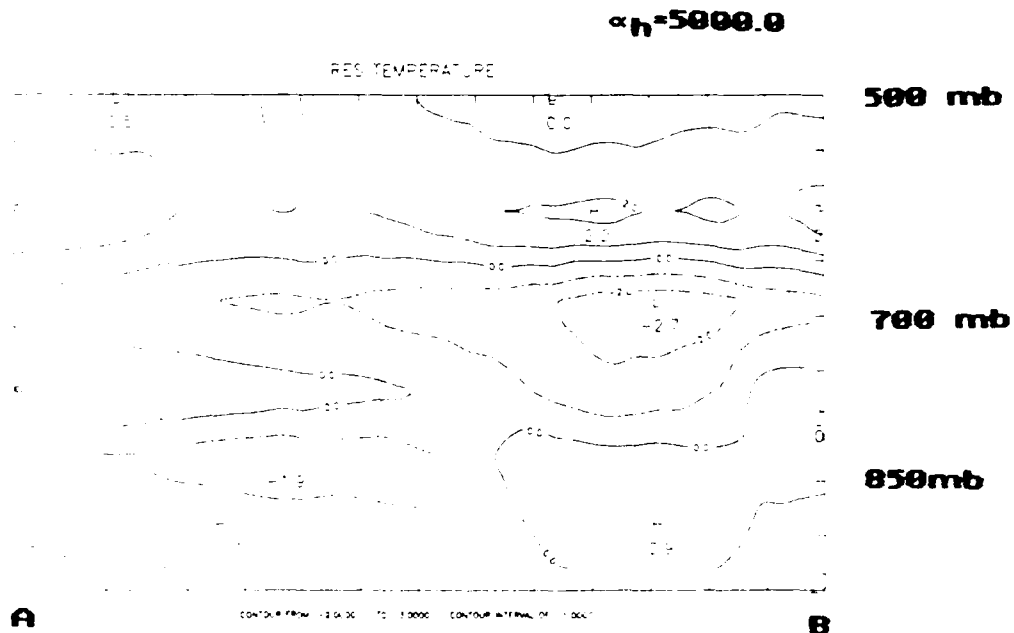
Fig 16b   Weight test α_h=5000.

Fig 16a-b   Test for hydrostatic temperature error module α_h. 16a shows ahydrostatic temperature found with std α_h. 16b shows same with std $\alpha_h \ast 100$

fields are found in Appendix A.

CHAPTER V

RESULTS

Many of the results shown in this section will be
in the form of vertical cross-sections of the analysis
grid. These cross-sections represent vertical slices taken
along line A-B in Fig 17. There are 15 gridpoints in the
horizontal along this line and 10 gridpoints in the vertical
extending from 950 mb to 500 mb. Approximate station
locations close to line A-B will be shown along the
bottom of the plots as well as the approximate surface
frontal position. There will be two types of
cross-sections shown. The first type, labelled original,
includes only data from gridpoints closest to the vertical
cross-section. In the second type, labelled average, each
gridpoint in the cross-section represents data averaged
along the curves shown in Fig 17 at all levels. These
curves are positioned to be approximately parallel to
the front. The intent of such averaging is to eliminate
small deviations present along the front and determine
which features are representative of the front as a
whole. Deviations are predicted along a density interface
by the work of Simpson (1972) whose experiments show
the formation of clefts and lobes in the frontal surface

38
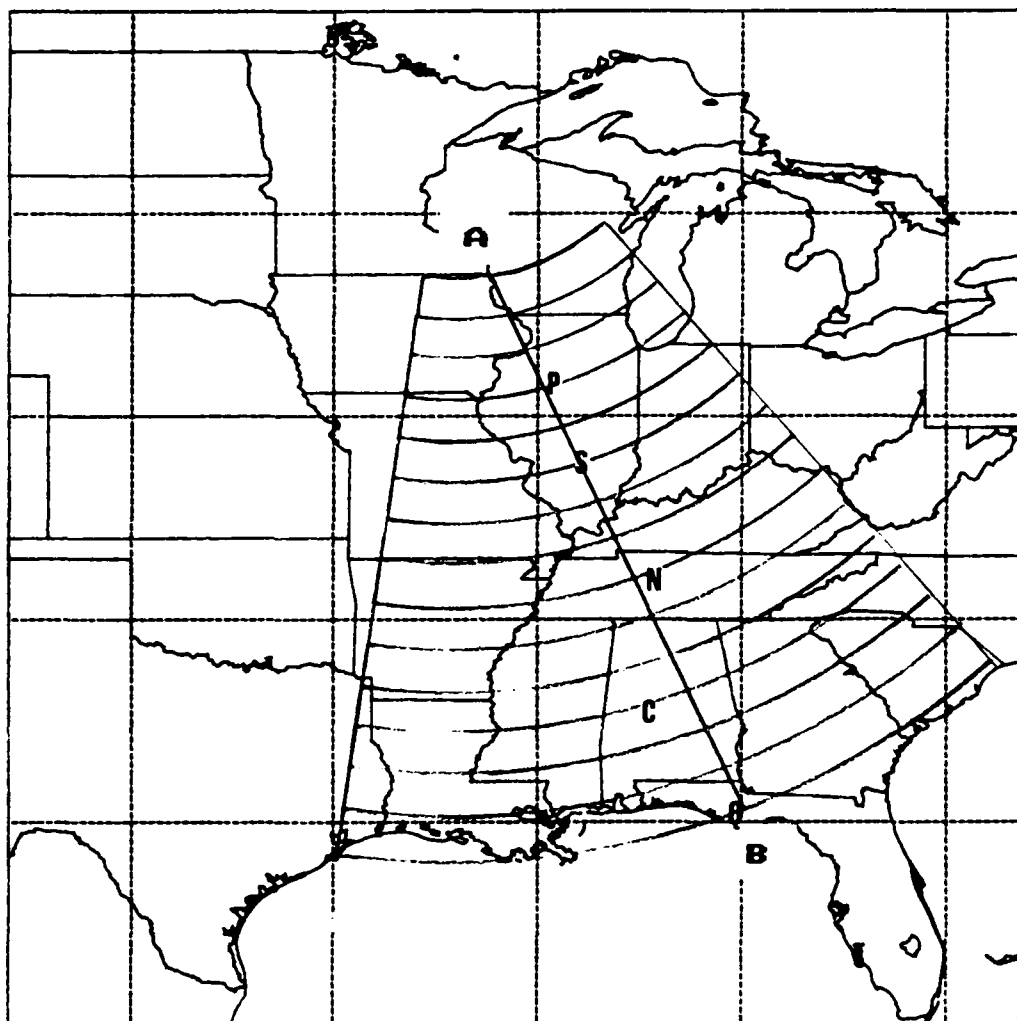
Fig 17   Horizontal analysis grid showing projection of
vertical cross-section line A-B. The curves are used for
averaging along the front. The intersection of the
curves and line A-B shows horizontal position of
gridpoints in vertical cross-section.

Station locations close to vertical cross-section line A-B
are listed on cross-section plots as P =Peoria   S =Salem
N =Nashville   C =Centerville   Q =Appalachacola.

of density currents. Tests were made with different
length averaging curves with no appreciable change in
the results. Fig 18 shows the barograph tracing for West
Palm Beach Fla. from Jan 26 to Jan 29, 1986. The three
times at which the radiosonde data were analyzed are
marked on the time series plot. The passage of the first
front is denoted by F1 on the tracing and that of the
CAO front is denoted by F2. This passage is preceeded
by a rise in surface pressure. At frontal passage there is
a dip in pressure and then a continued rise to a
maximum approximately 18 hours later. This maximum is
then followed by a sharp decrease in pressure. This
pattern is similar qualitatively to that of the gust front
passage pressure tendency shown in Fig 2a.

Figs 19a-c show the potential temperature (Θ)
profile along the original line for 00z27, 12z27, and 00z28
respectively. Fig 19a shows clearly the strong horizontal
gradient of Θ at the lowest level. The front at this time
is near Nashville (BNA). In Fig 19b, 12 hours later, the
front is between Centerville (CKL) and Appalachacola
(AQQ). The frontal position was determined at the
lowest level through examination of these plots and the
plots of relative vorticity. From this analysis it was
determined that the average propagation speed of the
front was approximately 11.6 m/s. In Fig 19b there is
evidence of the formation of the intense cold pool at
the southern tip of Illinois as there is significant lifting
of the isentropes locally in this area. This lifting can be

41
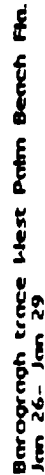
Fig 18   Barograph tracing from Jan 26-Jan 29,1986 at
West Palm Beach, Fla.. 1 hour time increments in inches
of mercury.

93   00Z/27/86   OR.G NAL

POTENTIAL TEMPERATURE
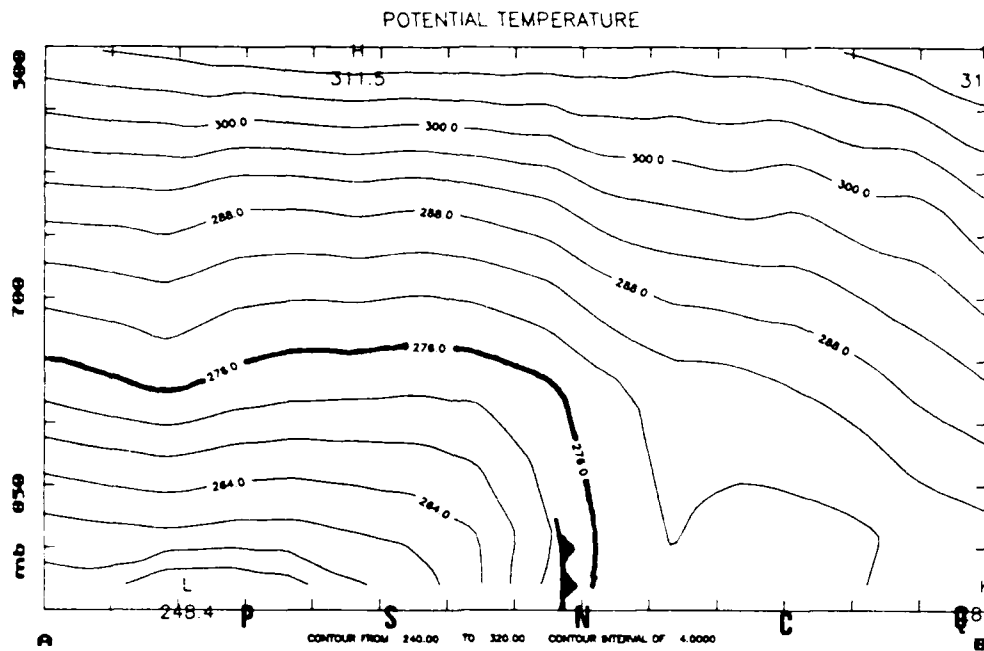
Fig 19a

93   12Z/27/86   ORIGINAL

POTENTIAL TEMPERATURE

Fig 19b

Figs 19a–b Potential temperature original cross–section in Kelvin for 00z Jan 27 and 12z Jan 27 respectively.

POTENTIAL TEMPERATURE

Fig 19c Potential temperature original cross-section in Kelvin for 00z Jan 28

POTENTIAL TEMPERATURE   AVERAGE
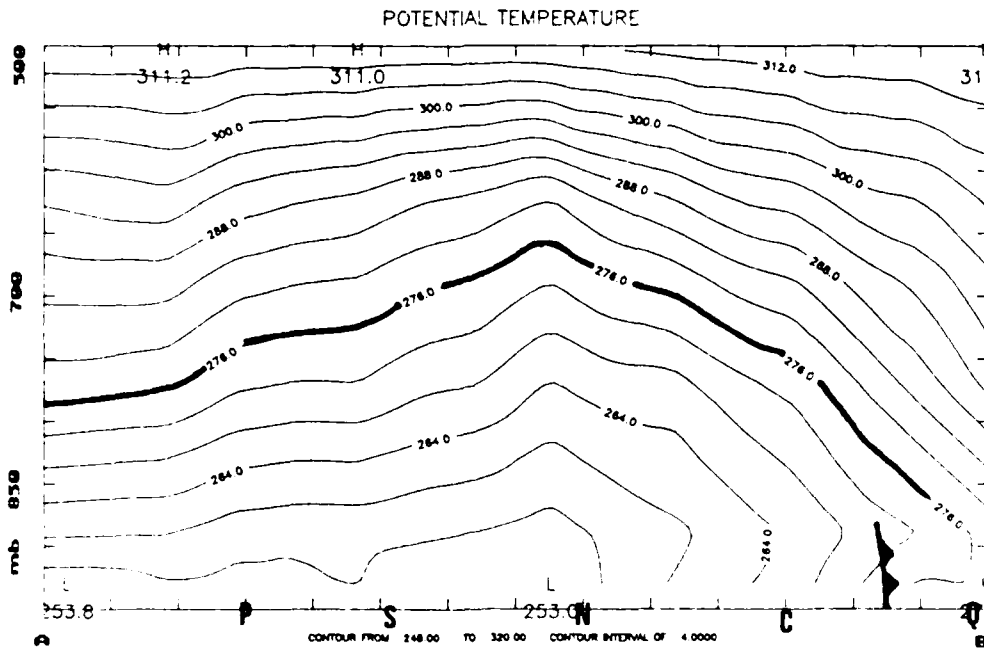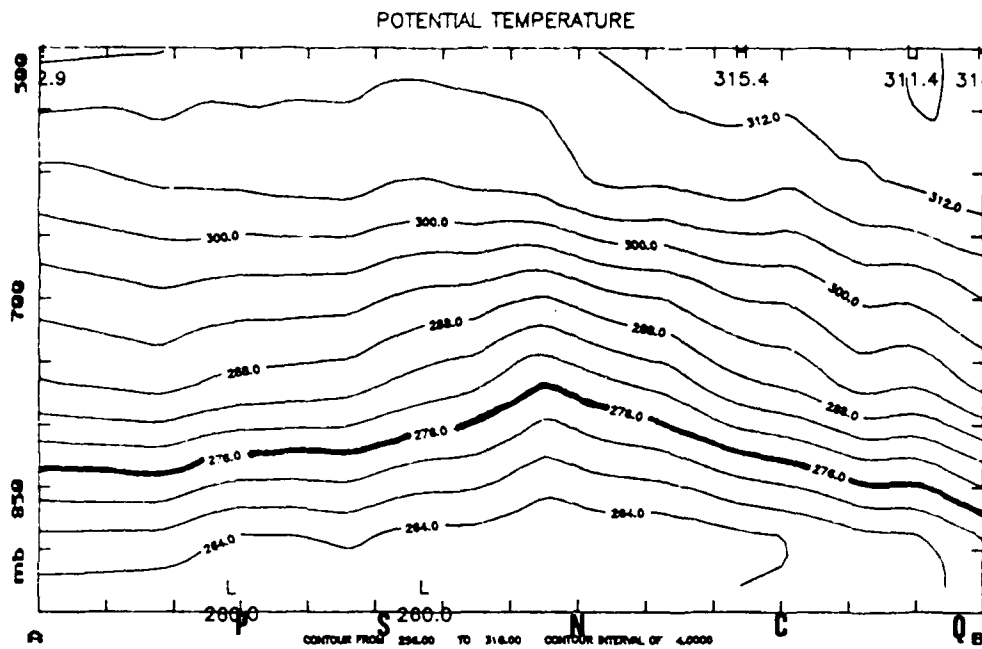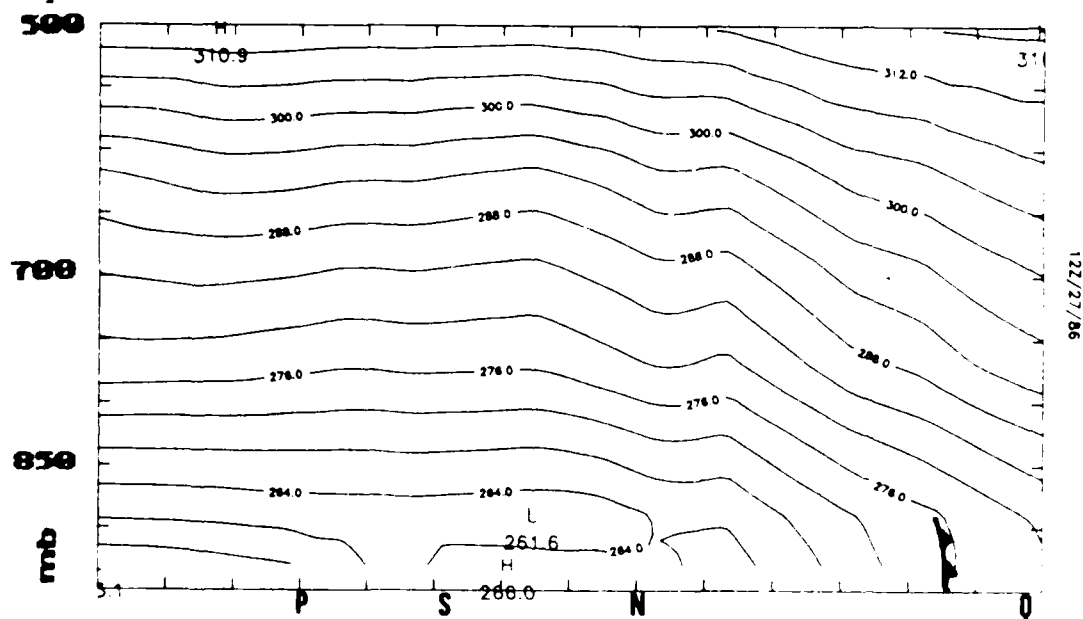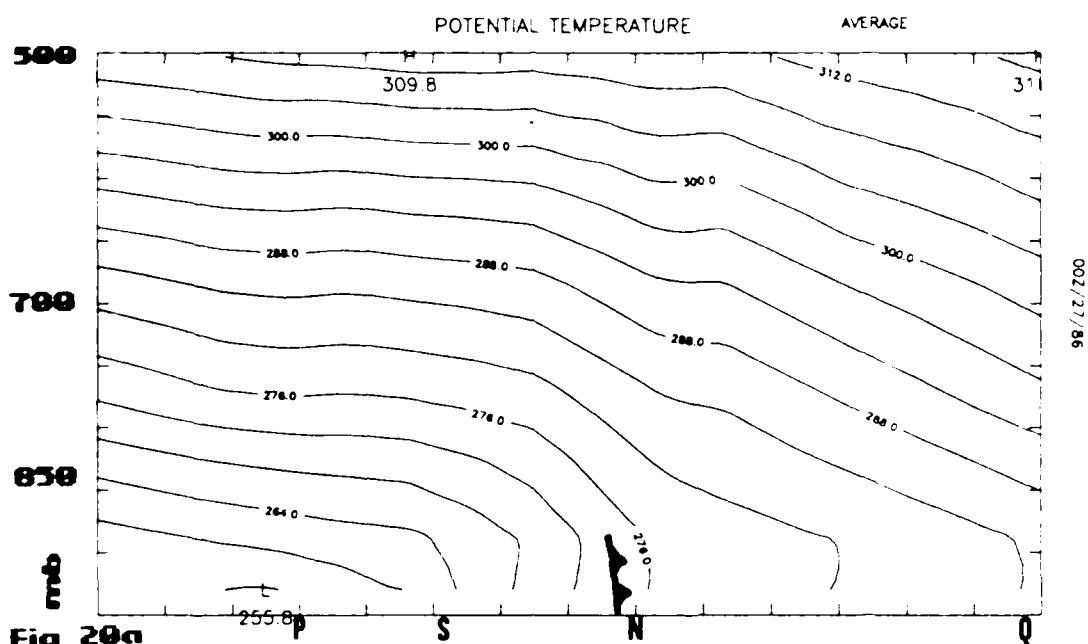

Fig 20a

Fig 20b

Figs 20a-b Potential temperature average cross-section in Kelvin for 00z Jan 27 and 12z Jan 27 respectively.
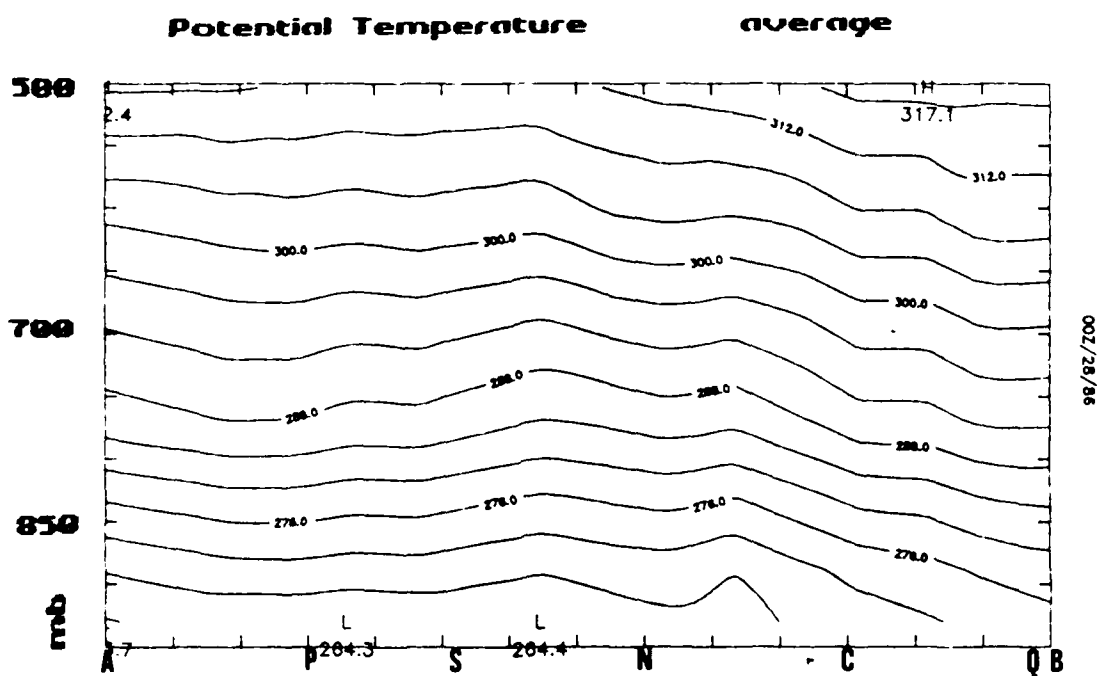
Fig 20c Potential temperature average cross-section in Kelvin for 00z Jan 28

seen by comparing the height of the 276 K isentrope (in bold) from 19a to 19b. Just behind the front in this plot there is an area of instability in the lowest level. In Fig 19c, although the isentropes are still somewhat higher in the Ohio Valley area, the isentropes have lowered in height from their positions at 12z27. Figs 20a-c are the same plots along the average line. The similarity of Figs 19a-c and Figs 20a-c, taking into account the expected smoothing done by the averaging process, suggests that the use of these averaging curves is justified.

The rising of the Θ surfaces from 0z27 to 12z27 and their subsequent lowering between 12z27 and 0z28 suggests that the potential energy of the area may be changing during this period. Figs 21a-c indicate that this is indeed the case. The potential energy was determined by integrating the product of the observed density ρ and geopotential ϕ in a vertical column from level 2 through level 8 at each point in the horizontal grid. The maximum value in each plot corresponds roughly with the location of the surface high. Fig 21b shows that a ridge of high potential energy forms in the Ohio Valley as a trough of low potential energy forms along the front. Fig 21c shows that this ridge remains intact at 0z28 while the trough is no longer evident. The front at this time has now moved off the grid to the southeast. This increase in potential energy seems to be due to three main causes. The first is the very cold temperatures that form in this area as shown before in
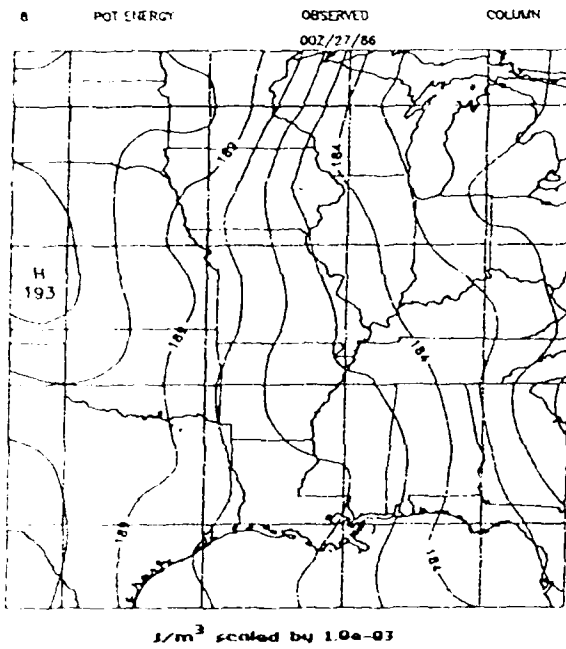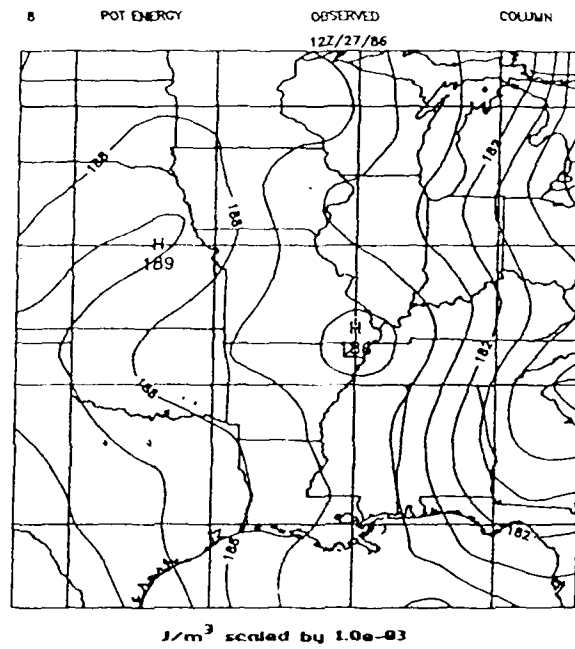
Fig 21a

Fig 21b
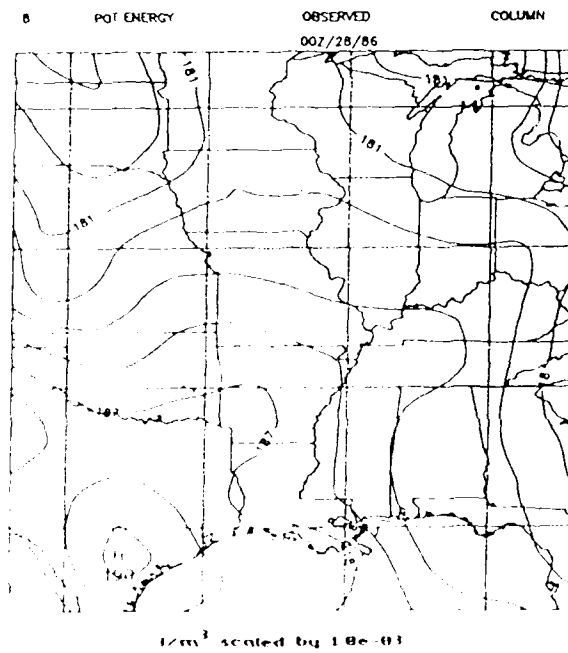
Fig 21c

Figs 21a-c Potential energy in vertical column from 922 mb to 354 mb for 00z Jan 27, 12z Jan 27, and 00z Jan 28.

Figs 14-16. The formation of this cold pool was discussed earlier and was largely due to synoptic scale forcing. The second main cause is illustrated in Fig 22 which shows the vertical velocity field at 12z27 computed using the Q-vector form of the quasi-geostrophic omega equation. This plot indicates that this area of rising potential energy was subject to fairly strong synoptic scale lifting apparently due to strong differential advection of cyclonic vorticity. This would tend to increase the potential energy by raising the center of gravity. The third cause is illustrated in Fig 23 which shows the average observed cross-front winds, the component of the average observed winds parallel to line A-B, at 8z27. This plot shows the winds behind the front to be 16 m/s while the frontal speed was 11.6 m/s. The ratio of these values is 1.37 which is in agreement with that found for a density current by Simpson (1969). The resultant convergence can also contribute to the rising motion of the area and thus to the increase in potential energy. It is important to note that although the first two factors described are synoptic in nature and seem to be most ective in the Ohio Valley during all three time periods, the last effect is tied to the position of the front and therefore moves with the front.

The next fields of interest are the AGEO heights and AGEO winds as described in the variational method section. Figs 24a-b show the average AGEO winds as

5   OMEGA   QUAS—GEO   850 MB

12Z/27/86
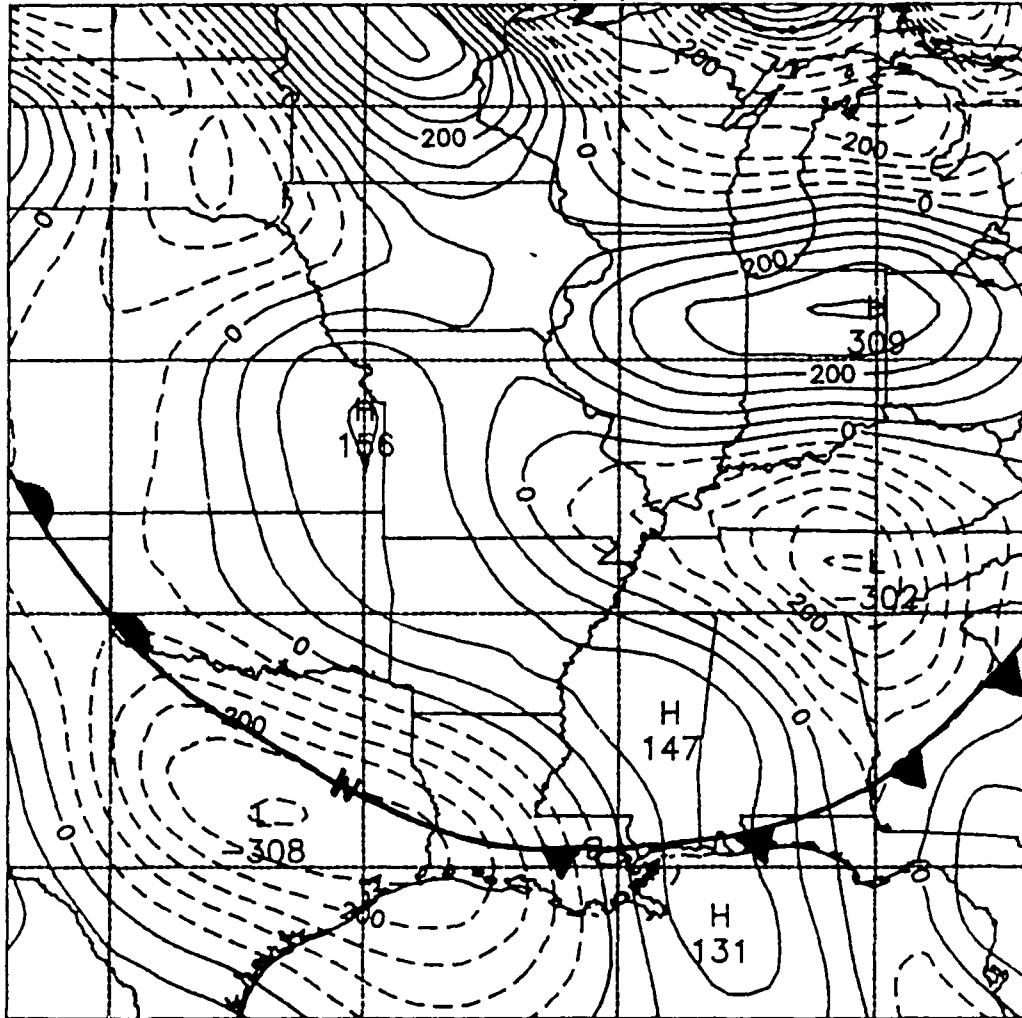
Pa/s scaled by 1.0e+04

CONTOUR FROM —0.45000E—01 TO 0.40000E—01 CONTOUR INTERVAL OF 0.50000E—02 PT(3,3)= 0.23118E—02 LABELS SCALED BY 10000.

**Fig 22 Quasi-geostrophic ω (dp/dt) calculated at 850 mb
12z Jan 27.**

104   00Z/27/86   AVERAGE

OBS CROSS FRONT WINDS
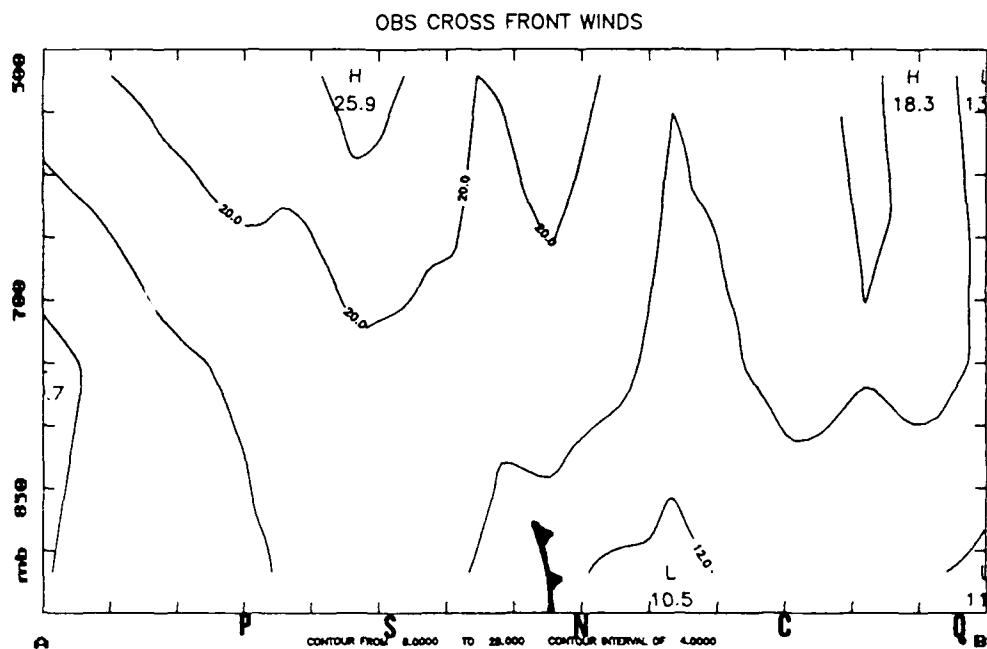
Fig 23   Observed cross front winds for 00z Jan 27 average cross-section in m/s.

Fig 24a   Longest vector is 7.3 m/s

Fig 24b   Longest vector is 25.8 m/s
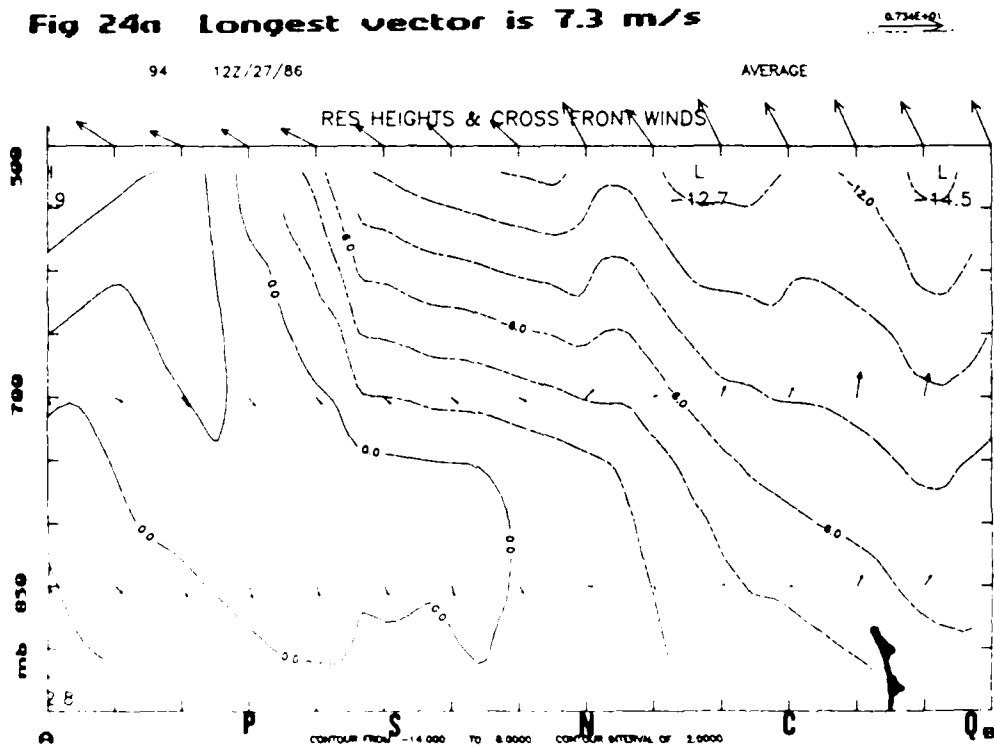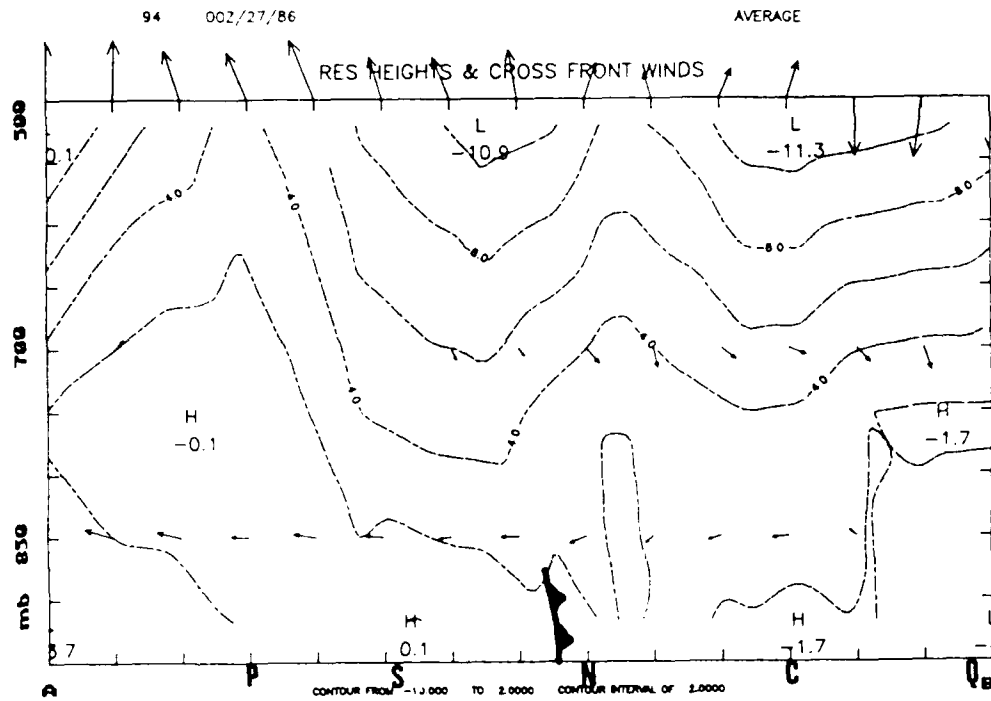
Figs 24a-b   Contours are ageostrophic heights in meters, barbs are ageostrophic winds for 00z Jan 27 and 12z Jan 27 average cross-section.

barbs superimposed on the plot of the average AGEO heights for 0z27 and 12z 27 respectively. Fig 24a shows a ridge in the AGEO heights at the front with a trough just behind the front and a more pronounced ridge further back. Fig 24b shows that 12 hours later the ridge is still evident behind the front, but the trough has now moved ahead of the front. It is speculated that this strong ridge of AGEO heights is analogous to the head of a gravity current. The smaller ridge which preceeded the front may be analogous to the density surge at the leading edge of a gust front. The AGEO winds in Fig 24a show an indirect circulation present at 0z27 with sinking motion on the warm side and rising motion on the cold side. This pattern is recognized as being frontogenetic because it tends to increase the temperature gradient through adiabatic warming on the warm side and adiabatic cooling on the cold side. The AGEO winds in Fig 24b show that at 12z27 the circulation has reversed and now the circulation is direct and frontolytic. The reversal of the AGEO circulation can be explained by the interaction of the AGEO vorticity (ζa) with the divergence (D) as discussed in the introduction. Fig 25a is the average cross-section of ζa for 00z27 and indicates that since the rate of change of D following the motion of the front is proportional to ζa, the resultant forcing of D by ζa at 00z27 will create divergence where ζa is positive behind the front and will create convergence where ζa is negative ahead of the

96   00Z/27/86   AVERAGE
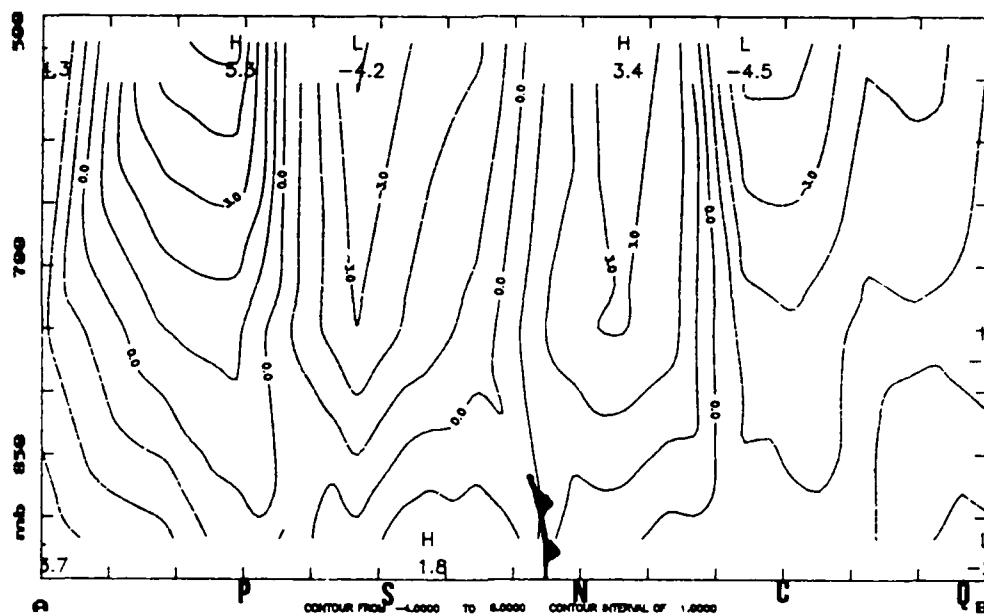
AGEO VORTICITY   s^{-1} scaled by 1.0e+05

Fig 25a

RES DIVERGENCE   s^{-1} scaled by 1.0e+05
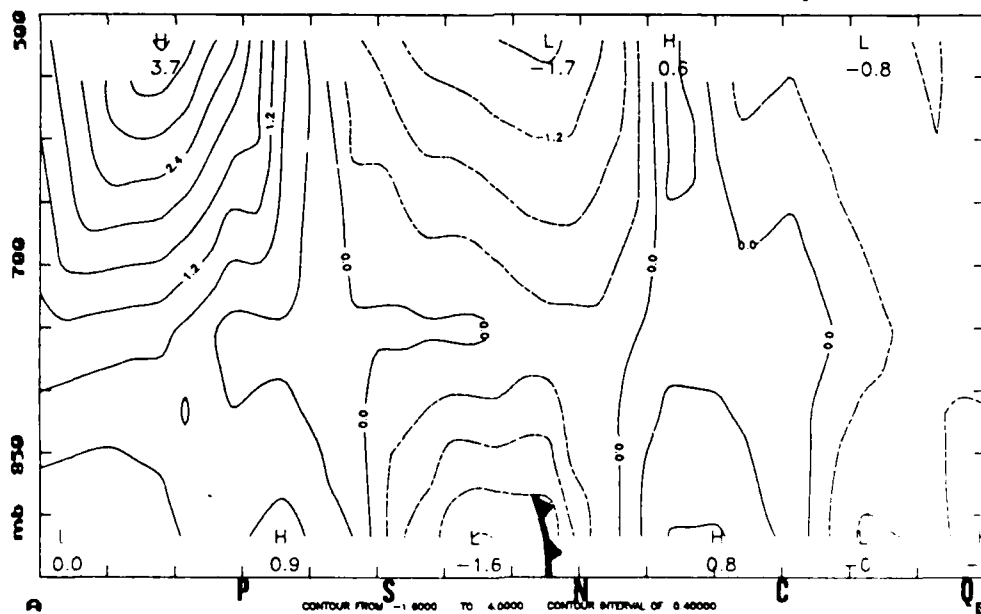
Fig 25b

Figs 25a-b   Contours of ageostrophic vorticity and divergence for 00z Jan 27 in average cross-section.

front in the lower levels. Since the ζ_a pattern is
reversed in the upper levels the resulting divergence
pattern will be reversed also. The circulation forced by
such a divergence-convergence pattern would indeed be
that exhibited in the AGEO winds of 12z27. Therefore it
seems that although in the first time period, the AGEO
winds are acting frontogenetically, the AGEO vorticity
field is acting to reverse the circulation and is thereby
limiting the frontogenetic process. Calculations of the
average geostrophic deformation near the front also
show that the term $F\zeta_a$ is at least one to two orders of
magnitude larger than the deformation terms in the
divergence equation at this time. Therefore it seems
possible that ζ_a may indeed be a controlling factor in
the frontogenetic process. It is further speculated that
the direct circulation found in the AGEO winds of 12z27
is analogous to the roll circulation found in the head of
a gravity current by Simpson (1969) and Charba (1974),
shown in Fig 2c.

Fig 25b is the average cross-section of the
divergence field calculated using the AGEO winds at 8z27
and shows a broad area of convergence through the
layer near the front. Comparison of 25a with 25b shows
that near the front, the divergence field does indeed
lead the ζ_a field. In the area above 850 mb at BNA the
zero line of ζ_a runs almost directly through the center
of the convergent area. This is to be expected because
the frontogenetic process is already strong at this time

and a strong horizontal temperature gradient already exists. According to the hypothesis of OR this phase shift between the two fields would allow an existing front to exist relatively unchanged following its motion with ζ_a providing just enough influence to counteract the other terms in the divergence equation. In the layer below 850 mb at the front ζ_a is almost 180 degrees out of phase with D. Here ζ_a directly opposes the stronger frontogenetic forces present at the front near the surface. Note also that the difference in the wavelengths of D and ζ_a is much greater at the lower levels than at the upper levels. This suggests that not only the phase shift between these two fields is important, but also their respective wavelengths as well.

Figs 26a-b show the same fields for 12z27. At the front there is a similar pattern with ζ_a and D far out of phase in the lowest level while closer to 90 degrees out of phase higher up. Note that in all cases the divergence field found in Fig 26b correlates well with ζ_a from the time before, shown in Fig 25a, following the motion of the front. Behind the front between Peoria (PIA) and Salem (SLO) D is directly in phase with ζ_a which enhances the development of divergence in this area and enhances convergence just northwest of PIA. Figs 27a-b show the same fields for 0z28. In this time period there is convergent area centered at 650 mb over BNA with the zero line of ζ_a running directly through it and a divergent center just north of PIA at the same level
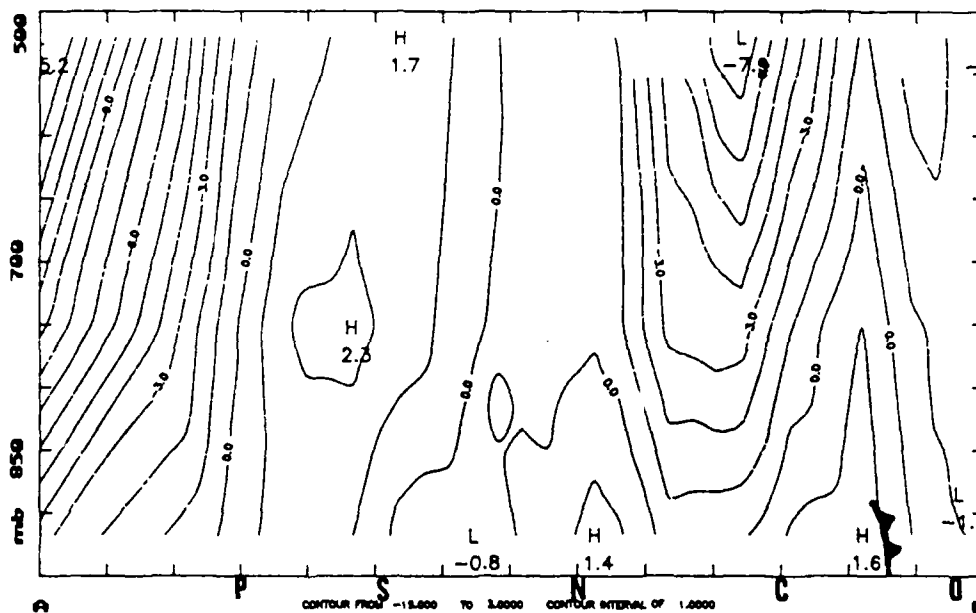
Fig 26a

Fig 26b

Figs 26a–b Contours of ageostrophic vorticity and divergence for 12z Jan 27 in average cross-section.

96   00Z/28/86   AVERAGE
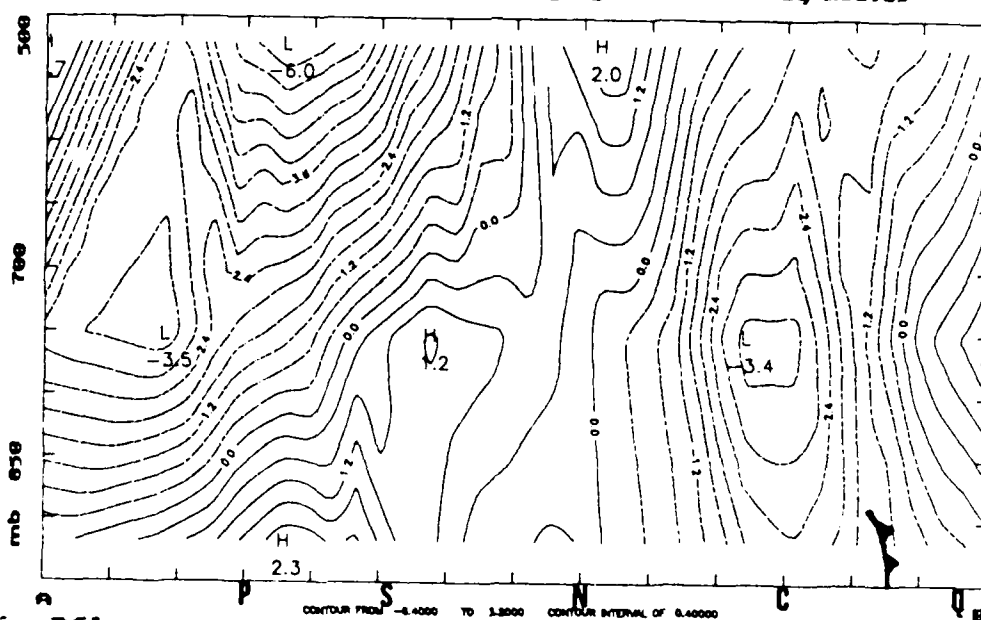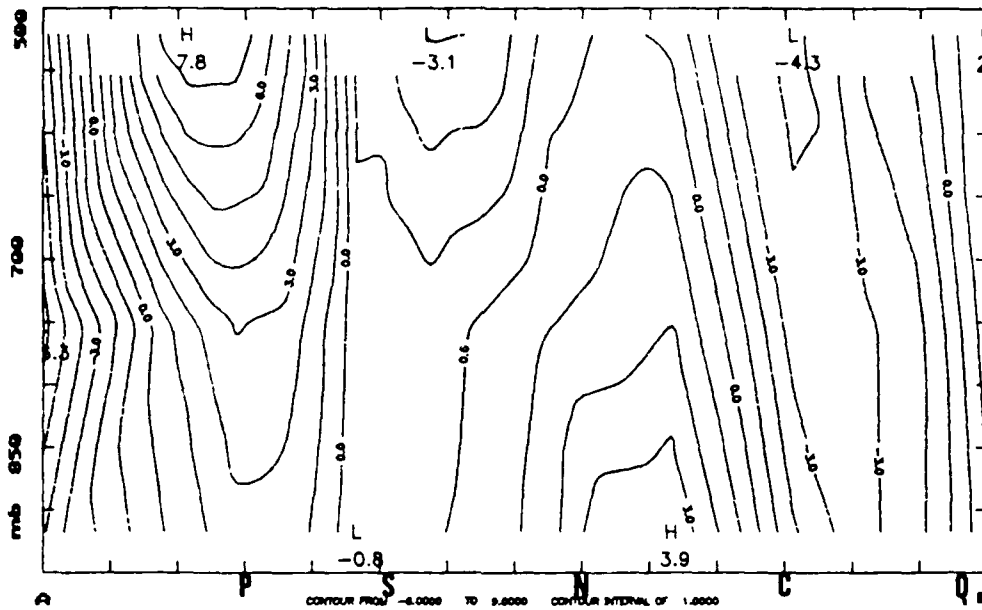
AGEO VORTICITY   s⁻¹ scaled by 1.0e+05

Fig 27a

RES DIVERGENCE   s⁻¹ scaled by 1.0e+05
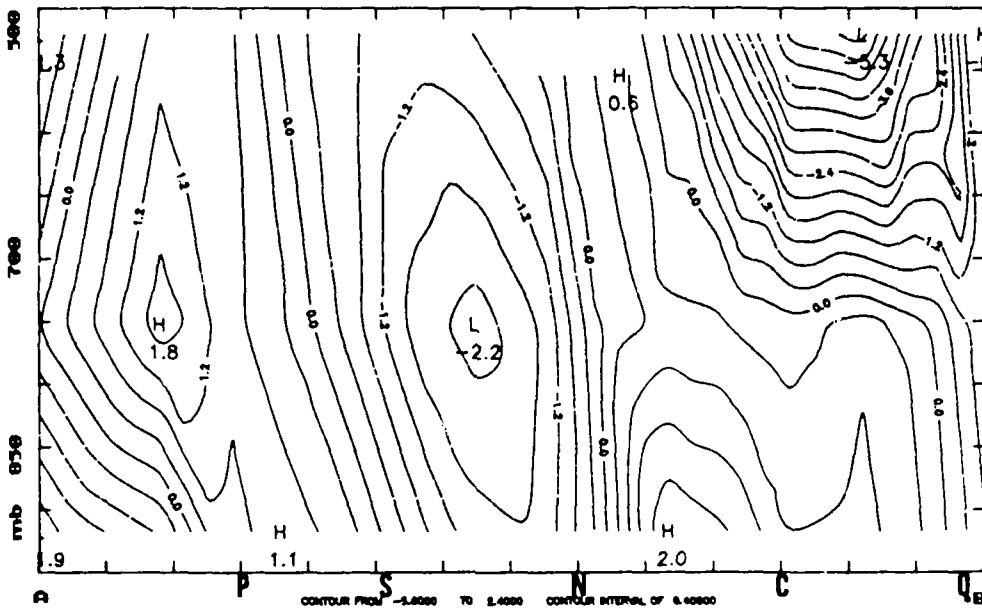
Fig 27b

Figs 27a-b   Contours of ageostrophic vorticity and divergence for 00z Jan 28 in average cross-section.
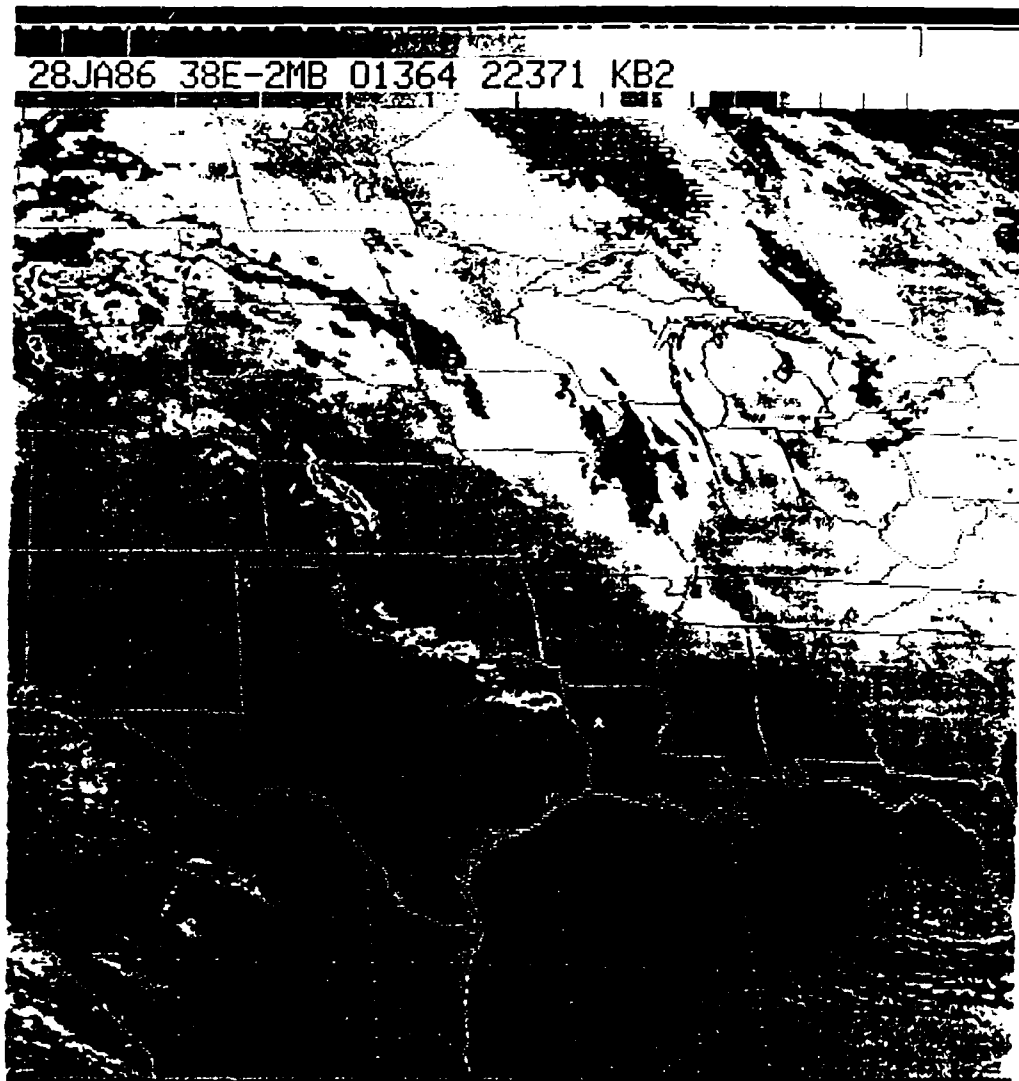
Fig 28 Infra-red satellite photo from 0001z Jan 28, 1986 showing high cloud tops near SLO.

with a zero line of ζ_a running directly through it. This would indicate that after the front has passed, the influence exerted by ζ_a on D diminishes. This pattern seems to be validated by the satellite photo, Fig 28, from 0z28 which shows an area of high cloud tops over the area of convergence shown in Fig 27b.

Figs 29a-c are the average cross-sections of the AHYD temperatures for 0z27, 12z27, and 0z28 respectively. As stated earlier, the AHYD temperature represents temperatures that are unbalanced with the geostrophic-hydrostatic state. Fig 29a shows a high in front of the front which slopes back over the frontal zone. This feature may be caused by the strong subsidence evident near the front in Fig 24a and subsequent entrainment of this air into the frontal zone. Entrainment of air from the warm side into the frontal zone is predicted by the work of Sanders (1955) and is discussed further in the following section on inertial instability. The presence of the high at the front is also analogous to the thermal ridge reported to accompany gust fronts by Charba (1974) and Mitchell and Hovermale (1977). At the 700 mb level there is a stratified layer of low temperatures capped by a layer of high temperatures. In Fig 30b this pattern is seen to move with the front revealing a break in the layer of low temperatures with a high directly below the break. There seems to be a correlation between the AHYD temps here and the stability of the atmosphere since this break
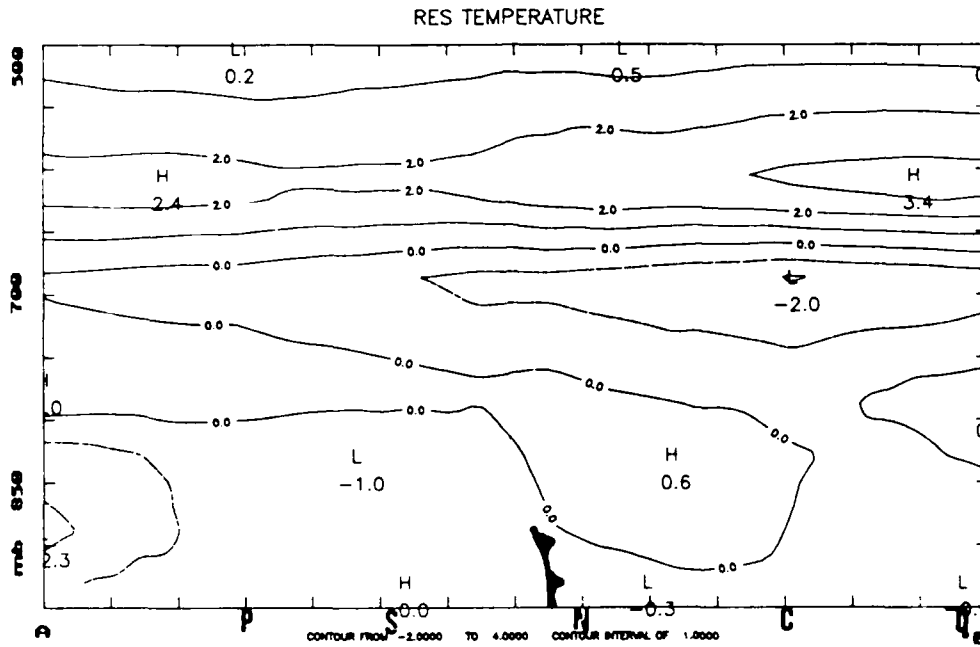
RES TEMPERATURE

Fig 29a

96   12Z/27/86   AVERAGE
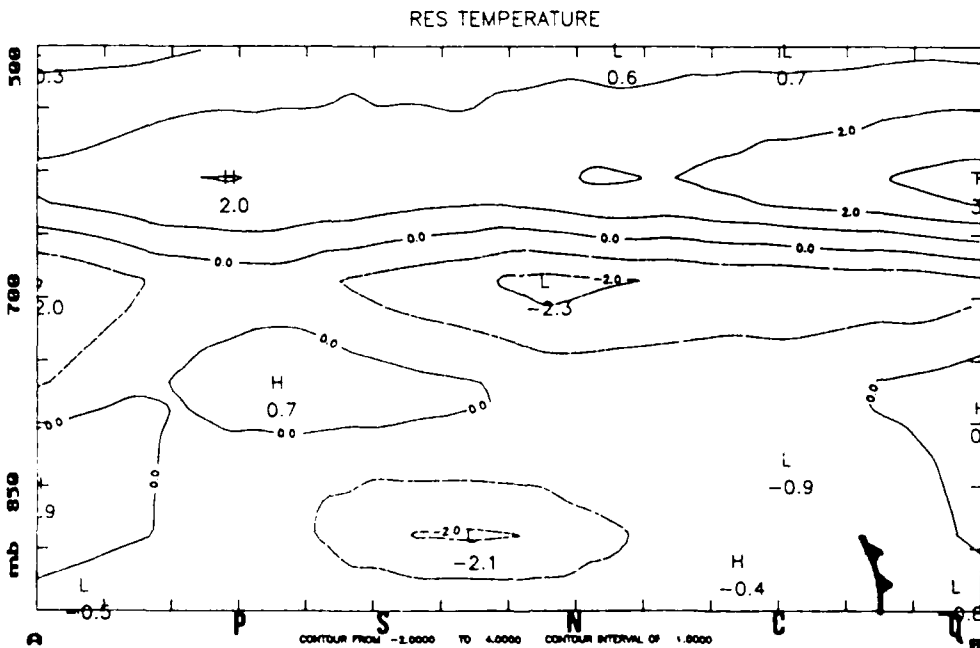
RES TEMPERATURE

Fig 29b

Figs 29a-b AHYD temperature average cross-section in Celsius for 00z Jan 27 and 12z Jan 27 respectively.

96   00Z/28/86   AVERAGE
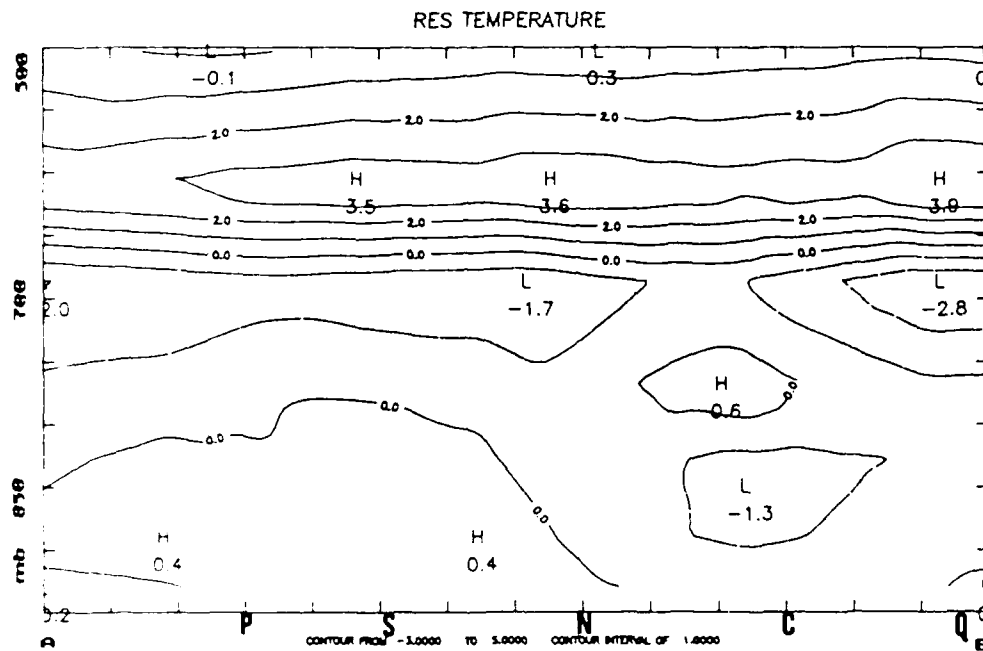
RES TEMPERATURE

Fig 29c AHYD temperature average cross-section in
Celsius for 00z Jan 28

occurs in the area of strong rising motion and high cloud tops. This is also an area in which gravity current studies indicate a mixing zone behind the head as shown in Fig 2c from Charba (1974). This mixing down of the warmer temperatures from above may also be a possible explanation for the break in the layer of low temperatures at the 780 mb level. Fig 30c again shows the pattern to be very persistent as the pattern is almost unchanged following the motion of the front. Further behind the front in Fig 29c the pattern becomes stratified.

Inertial Instability

Holton's reference text on dynamics (1978) states that inertial instability is present when the geostrophic absolute vorticity (ζab) becomes negative. This inertial instability will result in horizontal mixing until the area is again in a state of inertial stability. This relation is given by the expression

$$\zeta ab = f + \text{Geostrophic Relative Vorticity } (\zeta g)$$

$$\zeta ab = f+(dv_g/dx-du_g/dy)$$

where if

ζab >0   the atmosphere is inertially stable

=0   "   "   neutral

<0   "   "   unstable

where f is the Coriolis parameter and u_g and v_g are the components of the geostrophic wind. Since f is always positive in the northern hemisphere we can see
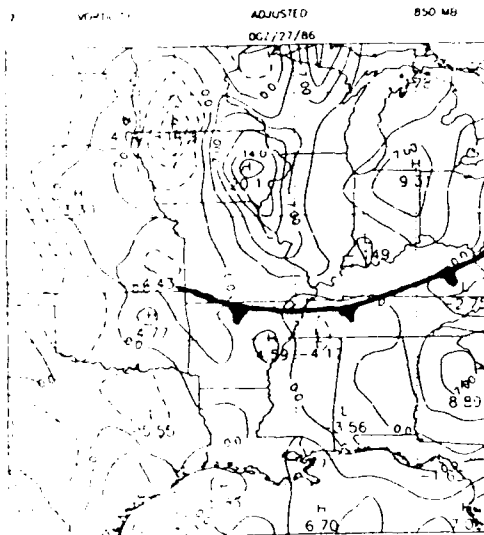
Fig 30a   850 mb
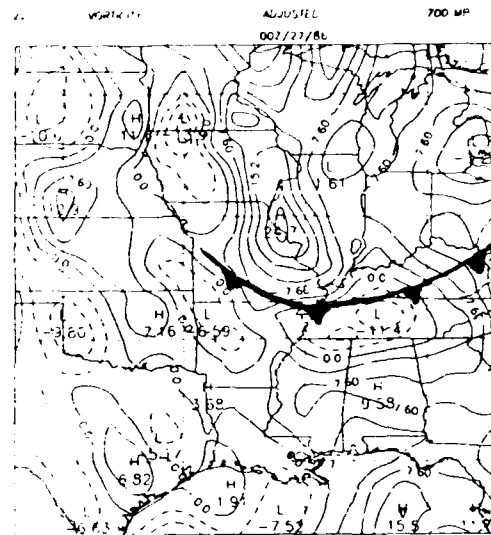
Fig 30b   700 mb
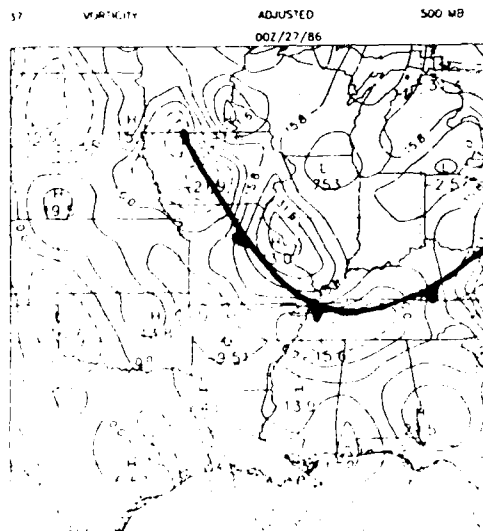
Fig 30c   500 mb

Figs 30a-c   Geostrophic relative vorticity scaled by
$1.0E+05$ in s^{-1} for 00z Jan 27.

64
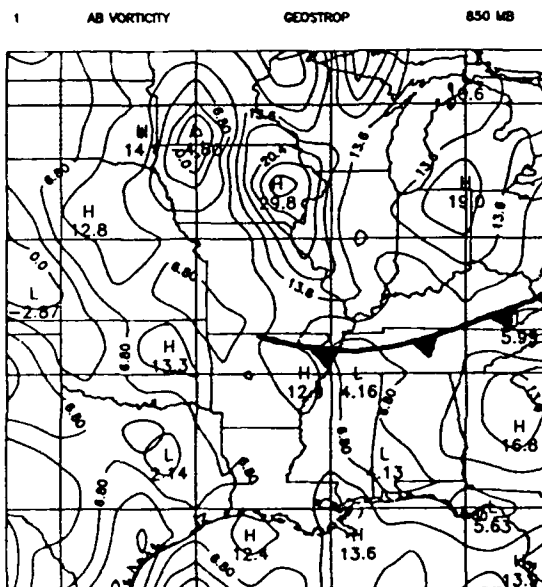
Fig 31a   850 mb
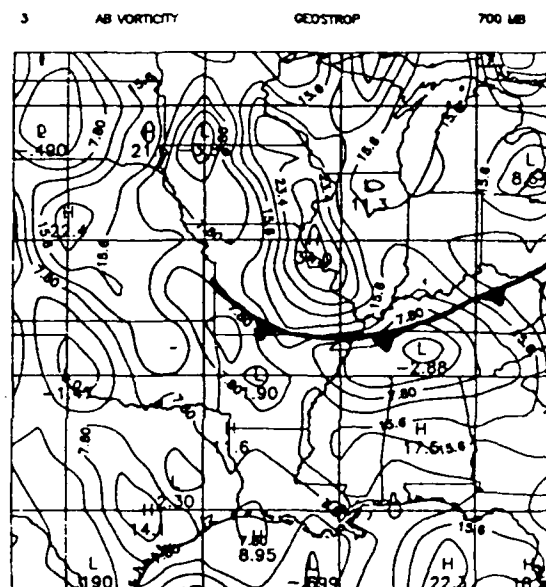
Fig 31b   700 mb
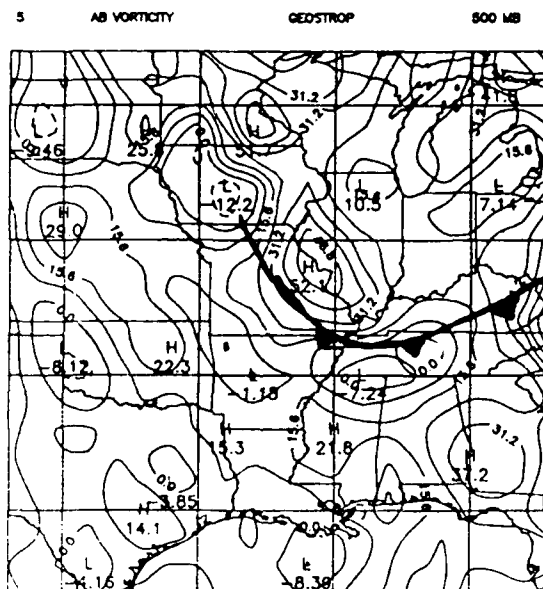
Fig 31c   500 mb

Figs 31a-c   Geostrophic absolute vorticity scaled by
1.0E+05 in s^{-1} for 00z Jan 27.

that where the ζ_g is negative we have the possibility of inertial instability. Figs 30a-c show the plots of the ζ_g for 0z27. Here we see that along the frontal zone at the edge of the cold pool (see Fig 6) ζ_g is indeed negative and of the same order of magnitude as f. Figs 31a-c are the plots of ζ_{ab} as described above. Fig 31a shows that at 850 mb there is a broad band of low values of ζ_{ab} along the frontal zone followed by an area of high values of ζ_{ab} centered over Eastern Iowa. From this it is evident that at the 850 mb level, the ζ_{ab} is nearly an order of magnitude less on the warm side of the front than on the cold side. This pattern is evident in all three levels. Since f is constant in a vertical column, and the geostrophic wind increases along the frontal zone due to the thermal wind relation these maximums and minimums grow more intense with height indicating areas of negative ζ_{ab} near the front. These plots indicate that the area just to the warm side of the front is inertially unstable causing horizontal mixing and thus entrainment of warm air into the frontal zone. Because this mechanism produces entrainment only on the warm side of the front, these results are in qualitative agreement with those presented by Sanders (1955). These results are also supported by the pattern of high AHYD temperatures extending along the frontal zone in Fig 29a.

CHAPTER VI

CONCLUSIONS

Comparison between the front associated with a CAO and a mesoscale gust front is hampered by the overwelming difference in scales. The CAO is so obviously dominated by synoptic forcing that it is difficult to see the similarities and perceive the subtle yet important effect the gravity current can have on this feature. A gust front has a spatial and temporal scale that does not allow the effects of the earth's rotation to be manifested to any large degree so its' gravity current aspects can be seen in the observed fields. Thus the head of a gust front is seen as an elevated area of high density air moving behind the front. The head has a roll circulation in it with considerable turbulence and mixing evident in the upper levels just behind the elevated head. In the CAO case it has been shown that behind the front there also exists an elevated area of high density air which exhibits itself as a ridge in the AGEO height field. This ridge also travels with the front keeping the same orientation. It has been shown that a roll circulation forms with the CAO front exhibited in the AGEO winds that moves in the

66

same sense as the roll circulation in the gust front head. The AHYD temperature field gives evidence of the existence of both an area of mixing behind the head and the presence of a thermal ridge at the leading edge as is evident in the gust front cases presented. In the CAO case these features are evident not in the observed fields as is the case of a gust front, but in the component of the observed fields that is unbalanced with the geostrophic-hydrostatic state.

As stated earlier, Hoskins and Bretherton (1972) showed that a front could be formed using semi-geostrophic theory, but the mechanism for controlling the frontogenetic process was incomplete. OR showed mathematically that the ageostrophic vorticity could control this process through its relative position and strength with respect to the divergence field. The results of this analysis seem to support this theory. OR speculated that gravity waves might have a role in the positioning of the divergence field while the vorticity field may be controlled by the synoptic system. Indeed the oscillatory nature of the divergence field suggests that gravity waves may have an important role here. If, however, the existence of gravity current effects are presumed, as the evidence suggests, a simpler controlling mechanism may be implied.

As the front forms, it has been shown in this case that the potential energy rises behind the front. This rise in potential energy is due at least to the denser air

behind the front but may also be due in part to
synoptic scale lifting and convergence in the lower
levels as in this case. A pressure gradient forms due to
this denser air which is partially balanced by the coriolis
force. As the front gets more intense, the pressure
gradient gets stronger which may become unbalanced
with the geostrophic state. When this occurs gravity
current features form in the ageostrophic components
as the results here indicate. As this current pushes
outward it carries with it the characteristic convergence
present at the leading edge of a density current. Since
the gravity current cannot influence the vorticity field
because it is basically irrotational in the horizontal
plane, this convergence then outruns the ageostrophic
vorticity field causing the phase shift required to
balance the frontogenetic process. There is evidence of
this overrunning in Figs 24a and 24b which show that
although the ridge in the AGEO height field shows no
appreciable movement with respect to the front, the
trough that was just behind the front in Fig 24a
becomes more intense and moves just ahead of the
front in Fig 24b 12 hours later. Also the observed phase
shift between D and ζa is greatest in the lowest levels
as one would expect if the gravity current effects were
forcing the phase shift.

The idea of a gravity current exhibiting itself in
ageostrophic components is one that would be
impossible to hold without this type of analysis. Only

through a technique that allows both the heights and winds to adjust to the geostrophic state can an ageostrophic height field be defined. The inclusion of this quantity into our analysis opens up many possibilties for forming and testing hypotheses such as the one presented here. The proof of the existence of such a gravity current is by no means complete in this investigation. A further variational technique would be required for this which will be discussed in the future research section.

CHAPTER VII

FUTURE RESEARCH

In order to more accurately investigate the hypothesis formed during this investigation another filter could be derived using the same variational technique as used here that would extract the gravity current components from the AGEO components already found. This would require the development of a simplified set of equations that could describe this component and then the construction of a functional using these equations. There are several interesting questions that might be answered in this way.

The first most obvious question is that of the exact nature of the gravity current interaction. Without this type of analysis it would be impossible to prove the existence of such effects. Other possible avenues of research would be:

Do these effects occur only in CAO type fronts or are they a significant factor in all fronts?

What is the cause and exact nature and effect of the varying wavelengths found in the divergence and AGEO vorticity field?

Are there sub-synoptic forces which act

significantly on the AGEO vorticity field, or is it mostly forced by the synoptic system as supposed by OR?

What are the exact physical interpretations of the AGEO and AHYD components? What are the effects of altering the filtering process and/or sequence?

These are only a few of the questions raised by this investigation. Hopefully this project may have stimulated interest in this type of analysis so that more of them may be pursued in the future.

BIBLIOGRAPHY

Benjamin,T.B.,1968:Gravity Currents and Related
Phenomena. J.Fluid Mech.,31,201-248.

Berson,F.A.,1958:Some measurements on Undercutting Cold
Air. Quart.J.R.Met.Soc.,84,1-15

Charba,J.A.,1974:Application of Gravity Current Model to
Analysis of Squall Line Gust Front. MWR, 102,140-156.

Chiang,C.P.,et al,1983:Gravitational Character of Cold
Surges during Winter Monex. MWR,111,293-307.

Clarke,R.H.,1961:Mesostrucure of Dry Cold Fronts over
Featureless Terrain. Journal of Meteor.,V18
No6,715-735.

Daly,J. and Pracht,W.,1968:Numerical Study of Density
Surges.The Physics of Fluids,11-1,15-30

Haltiner,G. and Williams,R.,1980:Numerical Prediction and
Dynamic Meteorology. Wiley and Sons, 299-310

Holton,J.R.,1979:An Introduction to Dynamic
Meteorology,Academic Press,p215-216.

Hoskins,B.J.,and Bretherton,F.P.,1972 :Atmospheric
Frontogenesis Models:Mathematical Formulation and
Solution. JAS,29,11-37.

Martin,H.C.,1973:Some Observations of the

Microstructure of Dry Cold Fronts,
JAM,12,658-663.

Mitchell,K.E., and Hovermale,J.B.,1977:A Numerical
Investigation of the Severe Thunderstorm Gust
Front. MWR,105,657-675.

Orlanski,I. and Ross,B.,1984:The Evolution of an
Observed Cold Front. Part II:Mesoscale Dynamics,
JAS,41-10,1669-1703

Sanders,F.,1955:An Investigation of the Structure and
Dynamics of an Intense Surface Frontal Zone,
Journal of Meteor,12,542-552.

Shapiro,M.A.,1984:Meteorological Tower
Measurements of a Surface Cold Front,.
MWR,112,1634-1639.

Simpson,J.E.,1969:A Comparison Between Laboratory
and Atmospheric Density Currents,
Quart.J.R.Met.Soc., 95,758-765.

Simpson,J.E.,1972:Effects of the Lower Boundary
Condition on the Head of a Gravity Current,
J.Fluid Mech.,53,759-768.

Uccellini,L.W.,1975:A Case Study of Apparent Gravity
Wave Initiation of Severe Convective Storms,
MWR,103,497-513.

Williams,R.T.1967:Atmospheric Frontogenesis: A
Numerical Experiment. JAS,24,627-641.

Williams,R.T.,andPlotkin,J.,1968:Quasi-Geostrophic
Frontogenesis. JAS, 25,201-206.

APPENDIX A

HYDROSTATIC FILTER FINITE DIFFERENCE FORM

The vertical coordinate for the hydrostatic filter is the log pressure. Where R is the gas constant for dry air and PL is the pressure in mb.

$$P=-RLN(PL/1000)$$

The functional for the hydrostatic equation in finite difference form is   EQN 1)

$$J=\sum[\alpha(T_{ijk}-To_{ijk})^2+\beta(\phi_{ijl}-\phi o_{ijk})^2+\lambda_{ijk}$$

$$*(\phi_{ijk+1}-\phi_{ijk-1})/2\Delta P - T_{ijk})]\Delta P$$

where α is the error module for T and β is the error module for ϕ. These error modules are defined as $1/(T_1-T_0)^2$ where T_1 is the value of T at this iteration and T_0 is the value of T at the last iteration. All error modules are of this form. These error modules are also called weights and are recomputed upon each iteration. The value of these weights can alter the final value after the filtering process. The effect of changing these weights is handled in the text. λ is the lagrange multiplier for the constraint, HW (1980) The subscripts i j k indicate the gridpoint in x y and P respectively.

74

We want to minimize J, where

$$\delta J = \delta_T J + \delta_\phi J + \delta_\lambda J$$

from $\delta_T J = 0$ we get

$$2\alpha(T_{ijk} - T o_{ijk})\delta T - \lambda_{ijk}\delta T = 0 \quad \text{but } \delta T \text{ is small and}$$

arbitrary but not $= 0$

so

EQN 2)
$$T_{ijk} = \lambda_{ijk}/2\alpha + T o_{ijk}$$

From $\delta_\phi J = 0$ we get

$$\Sigma[\beta(\phi_{ijk} + \delta\phi_{ijk} - \phi o_{ijk})^2 + (\lambda_{ijk} + \delta\lambda_{ijk})($$

$$(\phi_{ijk+1} + \delta\phi_{ijk+1} - \phi_{ijk-1} - \delta\phi_{ijk-1}) - T_{ijk})$$

$$-\beta(\phi_{ijk} - \phi o_{ijk})^2 - \lambda_{ijk}((\phi_{ijk+1} - \phi_{ijk-1})/2\Delta P - T_{ijk})]\Delta P = 0$$

Combine terms

Neglect terms of order $(\delta)^2$ and use integration by

parts to get

$$2\beta(\phi_{ijk} - \phi o_{ijk})\delta\phi_{ijk} + \lambda_{ijk}(\delta\phi_{ijk+1} - \delta\phi_{ijk-1})/2\Delta P = 0$$

Integration by parts gives us the boundary condition

that $\delta\lambda = 0$ on the boundaries.

Expand this for $l=1$ to 9 and use the fact that $\delta\phi$ is

small and arbitrary but not $= 0$

$$2\beta(\phi_{ij1} - \phi o_{ij1}) - \lambda_{ij2}/2\Delta P_{2,1} = 0 \qquad\qquad\qquad k=1$$

$$2\beta(\phi_{ij2} - \phi o_{ij2}) + (0 - \lambda_{ij3})/\Delta P_{3,1} = 0 \qquad\qquad k=2$$

$$2\beta(\phi_{ijk} - \phi o_{ijk}) - (\lambda_{ijk+1} - \lambda_{ijk-1})/\Delta P_{k+1,k-1} = 0 \quad k=3,7$$

$$2\beta(\phi_{ij8} - \phi o_{ij8}) - (0 - \lambda_{ij7})/\Delta P_{9,7} = 0 \qquad\qquad k=8$$

$$2\beta(\phi_{ij9} - \phi o_{ij9}) - \lambda_{ij8}/2\Delta P_{9,8} = 0 \qquad\qquad\qquad k=9$$

Note that the finite difference form forces us to treat the equations differently near the boundaries. From this we get EQN 3) For k=2

$$\phi_2 = \lambda_3/2\beta\Delta PC + \phi o_2$$

EQN 4) For k=3,7

$$\phi_k = (\lambda_{k+1} - \lambda_{k-1})/2\beta\Delta PC + \phi o_k$$

EQN 5) For k=8

$$\phi_8 = -\lambda_7/2\beta\Delta PC + \phi o_8$$

The boundary condition that $\lambda=0$ at level 1 and 9 has been incorporated into these equations.

From $\delta_\lambda J=0$ we get

EQN 6) $((\phi_{ijk+1} - \phi_{ijk-1})/2\Delta P - T_{ijk}))\delta\lambda_{ijk}=0$
The original constraint

For ease of notation we will use

$$\Delta PC = P_{k+1} - P_{k-1}$$

$$\Delta PF = P_{k+2} - P_k$$

$$\Delta PB = P_k - P_{k-2}$$

$$\Delta PHT = P_k - P_{k-1}$$

$$\Delta PHB = P_{k+1} - P_k$$

From these we solve for T and ϕ in terms of To and ϕo and λ to get an expression for λ by substituting EQNS 1-4) into the original constraint EQN 5). We will drop the subscripts $_i$ $_j$ since all operations in the following expressions are performed over all i j.

$$(\lambda_{k+1}-\lambda_k)/2\beta\Delta PF\Delta PC - (\lambda_k-\lambda_{k-2})/2\beta\Delta PB\Delta PC$$

$$+(\phi o_{k+1}-\phi o_{k-1})/\Delta PC \ -\lambda_k/2\alpha-To_k = 0 \qquad \text{For } k=3,7$$

which simplifies to

For k=3,7   EQN 7)

$$\lambda_k=$$

$$\frac{[\lambda_{k+2}/2\beta\Delta PF\Delta PC+\lambda_{k-2}/2\beta\Delta PB\Delta PC+(\phi o_{k+1}-\phi o_{k-1})/\Delta PC-To_k]}{1/2\beta\Delta PF\Delta PC + 1/4\beta\Delta PHB\Delta PC + 1/2\alpha}$$

For k=2   EQN 8)

$$\lambda_k = \frac{[\lambda_{k+2}/2\beta\Delta PF\Delta PC + (\phi o_{k+1}-\phi o_{k-1})/\Delta PC - To_k]}{1/2\beta\Delta PF\Delta PC + 1/4\beta\Delta PHB\Delta PC + 1/2\alpha}$$

For k=8   EQN 9)

$$\lambda_k = \frac{[\lambda_{k-2}/2\beta\Delta PB\Delta PC + (\phi o_{k+1}-\phi o_{k-1})/\Delta PC - To_k]}{1/2\beta\Delta PB\Delta PC + 1/4\beta\Delta PHT\Delta PC + 1/2\alpha}$$

Once the appropriate λ is found we can calculate T and ϕ from EQNS 2-5).

GEOSTROPHIC FILTER

There are two functionals for the geostrophic constraint, one in u and one in v. These functionals are J1 in u and J2 in v. α is the error module of u and v and β is the error module of ϕ where

$$\alpha=1/(u-uo)^2 \qquad \beta=1/(\phi-\phi o)^2$$

EQN 10)

$$J1 = \sum_i \sum_j [\alpha(u_{ijl} - uo_{ijl})^2 + \beta(\phi_{ijl} - \phi o_{ijl})^2$$
$$+ \lambda_u (fu + (\phi_{ij+1l} - \phi_{ij-1l})/2\Delta y)] \Delta x \Delta y$$

EQN 11)

$$J2 = \sum_i \sum_j [\alpha(v_{ijk} - vo_{ijk})^2 + \beta(\phi_{ijk} - \phi o_{ijk})^2$$
$$+ \lambda_v (fv + (\phi_{i+1jk} - \phi_{i-1jk})/2\Delta x)] \Delta x \Delta y$$

$$\delta J1 = \delta_\phi J1 + \delta_u J1 + \delta_{\lambda u} J1 = 0$$

$$\delta J2 = \delta_\phi J2 + \delta_v J2 + \delta_{\lambda v} J2 = 0$$

so

$$\delta_\phi J1 = \sum_i \sum_j [2\beta(\phi_{ij} - \phi o_{ij})\delta\phi_{ij} + \lambda u_{ij}(\delta\phi_{ij+1} - \delta\phi_{ij-1})/2\Delta y] \Delta x \Delta y$$

$$\delta_\phi J2 = \sum_i \sum_j [2\beta(\phi_{ij} - \phi o_{ij})\delta\phi_{ij} - \lambda v_{ij}(\delta\phi_{i+1j} - \delta\phi_{i-1j})/2\Delta x] \Delta x \Delta y$$

$$\delta_u J1 = \sum_i \sum_j [2\alpha(u_{ij} - uo_{ij})\delta u_{ij} + \lambda u_{ij} f\delta u_{ij}] \Delta x \Delta y$$

$$\delta_v J2 = \sum_i \sum_j [2\alpha(v_{ij} - vo_{ij})\delta v_{ij} + \lambda v_{ij} f\delta v_{ij}] \Delta x \Delta y$$

$$\delta_{\lambda u} J1 = \sum_i \sum_j [\delta\lambda u_{ij}(fu_{ij} + (\phi_{ij+1} - \phi_{ij-1})/2\Delta y)] \Delta x \Delta y$$

$$\delta_{\lambda v} J2 = \sum_i \sum_j [\delta\lambda v_{ij}(fv_{ij} + (\phi_{i+1j} - \phi_{i-1j})/2\Delta x)] \Delta x \Delta y$$

After setting these to zero and expanding each, then recombining terms as we did in the hydrostatic case we get these working equations. Again we have used the fact that all δ quantities are small and arbitrary but not $=0$.

From $\delta_u J1 = 0$ we get

EQN 12) $$u_{ij} = uo_{ij} - (f/2\alpha)\lambda u_{ij}$$

and similarly from $\delta_v J2 = 0$ we get

EQN 13) $\quad v_{ij} = vo_{ij} - (f/2\alpha)\lambda v_{ij}$

These have no boundary problems.

When we do $\delta_\phi J1$ and $\delta_\phi J2$ we must account for the differences at the boundaries because of the derivative of ϕ in y and x. To do this we write out the expressions for $\delta_\phi J1$ for each possible j and solve for ϕ in each case this gives us 5 possible equations for ϕ depending on which row we are in.

EQN 14) $\quad \phi_{i1} = +(1/4\beta\Delta y)\lambda u_{i2} + \phi o_{i1}$ $\qquad$ for j=1

EQN 15) $\quad \phi_{i2} = +(1/4\beta\Delta y)\lambda u_{i3} + \phi o_{i2}$ $\qquad$ for j=2

EQN 16) $\quad \phi_{ij} = -(1/4\beta\Delta y)(\lambda u_{ij-1} - \lambda u_{ij+1}) + \phi o_{ij}$ $\quad$ for j=3,n-2

EQN 17) $\quad \phi_{in-1} = -(1/4\beta\Delta y)\lambda u_{in-2} + \phi o_{in-1}$ $\qquad$ for j=n-1

EQN 18) $\quad \phi_{in} = -(1/4\beta\Delta y)\lambda u_{in-1} + \phi o_{in}$ $\qquad$ for j=n

We can do the same operations for $\delta_\phi J2$ to get a similar equation for ϕ_{ij} for i=1,m-2

EQN 19) $\quad \phi_{ij} = -(1/4\beta\Delta x)(\lambda v_{i+1j} - \lambda v_{i-1j}) + \phi o_{ij}$

Now we plug the equations for u and ϕ into the equation for $\delta_{\lambda u} J1 = 0$ which is the geostrophic constraint in u.

$$\Sigma_i \Sigma_j \left[\delta \lambda u_{ij} \left[fuo_{ij} - (f^2/2\alpha) \lambda u_{ij} + (-1/4\beta \Delta y [\lambda u_{ij} - \lambda u_{ij+2}] + \phi o_{ij+1} \right. \right.$$

$$\left. \left. -1/4\beta \Delta y [-\lambda u_{ij-2} + \lambda u_{ij}] - \phi o_{ij-1})(1/2\Delta y) \right] \right] = 0$$

$$0 = [fuo_{ij} - f^2 \lambda u_{ij}/2\alpha - 1/8\beta \Delta y^2 (\lambda u_{ij} - \lambda u_{ij+2} + \lambda u_{ij} - \lambda u_{ij-2}) +$$

$$(\phi o_{ij+1} - \phi o_{ij-1})/2\Delta y]$$

We can solve this for λu_{ij} such that

EQN 20) $\quad \lambda u_{ij} = [2\alpha\beta(2\Delta y)^2][fuo_{ij} + (\lambda u_{ij+2} + \lambda u_{ij-2})/2\beta(2\Delta y)^2$

$$+(\phi o_{ij+1} - \phi o_{ij-1})/2\Delta y]/(f^2\beta(2\Delta y)^2 + 2\alpha)$$

This expression gives λu_{ij} in terms of λu_{ij} at other
locations and known quantities. We solve this iteratively
using the modified Newton-Rathson method.

The derivation of the equation for λv_{ij} is totally

analogous to that of λu_{ij} and yields

EQN 21) $\quad \lambda v_{ij} = [2\alpha\beta(2\Delta x)^2][fvo_{ij} + (\lambda v_{i+2j} + \lambda v_{i-2j})/2\beta(2\Delta x)^2$

$$+(\phi o_{i+1j} - \phi o_{i-1j})/2\Delta x]/(f^2\beta(2\Delta x)^2 + 2\alpha)$$

α and β are recomputed upon each iteration. First λu and

λv are computed and then u v and ϕ. The final values

after all iterations of u v and ϕ are then the geostrophic

components of these quantities.

EXTERNAL WAVE FILTER

This program uses the continuity equation to
exclude any external gravity waves from the final
components. The functional for this filter in finite

difference form is

EQN 22) $\sum_i \sum_j \sum_k \lambda_{kl}[(u-uo)^2+(v-vo)^2]\Delta P +$

$\lambda\sum((u_{i+1jk}-u_{i-1jk})/2\Delta x +(v_{ij+1k}-v_{ij-1k})/2\Delta y)\Delta P]\Delta x\Delta y=0$

I will drop all subscripts except those that are used in finite difference calculations since it is assumed the sums go over all points. Also since the constraint is independent of P we need to keep the integral in the constraint. If we expand this functional using variational calculus we get

$\sum[(u+\delta u-uo)^2+(v+\delta v-vo)^2]\Delta P$

$+(\lambda+\delta\lambda)\sum[(u_{i+1}+\delta u_{i+1}-u_{i-1}-\delta u_{i-1})/2\Delta x$

$+(v_{j+1}+\delta v_{j+1}-vo_{j+1})/2\Delta y]\Delta P$

$-\sum[(u-uo)^2+(v-vo)^2]\Delta P-\lambda\sum[(u_{i+1}-u_{i-1})/2\Delta x$

$+(v_{j+1}-v_{j-1})/2\Delta y]\Delta P=0$

Neglect terms of order $(\delta)^2$ to get

$2(u-uo)\delta u+2(v-vo)\delta v+\lambda\sum[(\delta u_{i+1}-\delta u_{i-1})/2\Delta x$

$+(\delta v_{j+1}-\delta v_{j-1})/2\Delta y]\Delta P$

$+\delta\lambda\sum[(u_{i+1}-u_{i-1})/2\Delta x+(v_{j+1}-v_{j-1})/2\Delta y]\Delta P=0$ $\delta\lambda( )=0$ gives

the original constraint

$\sum_p[(u_{i+1}-u_{i-1})/2\Delta x+(v_{j+1}-v_{j-1})/2\Delta y]\Delta P=0$

$\delta u( )=0$ gives

$2(u-uo)\delta u+\lambda\sum_p[(\delta u_{i+1}-\delta u_{i-1})/2\Delta x]\Delta P=0$

If we write these out for all possible i we get

$[2(u_1-uo_1)-\lambda_2/2\Delta x]\delta u_1=0$

$[2(u_2-uo_2)+(\lambda_1-\lambda_3)/2\Delta x]\delta u_2=0$

$[2(u_i-uo_i)+(\lambda_{i-1}-\lambda_{i+1})/2\Delta x]\delta u_i=0$

From this we get

EQN 23) $u_i = (\lambda_{i-1} - \lambda_{i+1})/4\Delta x + uo_i$

and similarly we get

EQN 24) $v_j = (\lambda_{j-1} - \lambda_{j+1})/4\Delta y + vo_j$

We plug these into the constraint equation to get

$$\Sigma_p[[(\lambda_i - \lambda_{i+2})/4\Delta x + uo_{i+1} - (\lambda_{i-2} + \lambda_i)/4\Delta x - uo_{i-1}]/2\Delta x$$

$$+[(\lambda_j - \lambda_{j+2})/4\Delta y + vo_{j+1} - (\lambda_{j-2} + \lambda_j)/4\Delta y - vo_{j-1}]/2\Delta y]\Delta P = 0$$

By rearranging terms we can solve for λ_{ij} in terms of λ

at other positions. Since λ in this case is not a function

of P we can remove it fron the sum to get

EQN 25) $\lambda_{ij} = [(\lambda_{i+2} + \lambda_{i-2})\Delta y^2 + (\lambda_{j+2} + \lambda_{j-2})\Delta x^2]/2(\Delta x^2 + \Delta y^2)$

$-2/P_s \Sigma_p[[(uo_{i+1} - uo_{i-1})\Delta y + (vo_{j+1} - vo_{j-1})\Delta x]$

$/(\Delta x^2 + \Delta y^2)]\Delta P$ Where P_s is $\Sigma_p\Delta P$

Here again we get λ in terms of known quantities and

other λ. We can solve this iteratively as before then

compute new values for u and v at each iteration. Note

that although λ is used as the lagrange multiplier in all

three filters, they are different in all three cases and

completely independent of each other.

CRESSMAN ANALYSIS

The weighting function is defined

$$W = \left(\frac{ROI2 - DK2}{ROI2 + DK2} \right) \quad \text{for } DK2 < ROI2$$

where

ROI2=ROI squared

DK2=DK squared

DK= the great circle distance between the gridpoint and the station location.

ROI= Radius of influence set at 495 km initially and then reduced by 10% on each successive pass. The values of 495 km and 10% were found to be optimal by testing different values and checking the station residuals at each pass. The station residual is the difference between the actual station value and the value found by using the same Cressman scheme to interpolate the gridpoint values back onto the station locations.

If DK2>ROI2 then the weighting function is set to 0. Gridpoint values are computed by adding the contributions from each station within the radius of influence by the formula

$$Value = \frac{\sum W Z}{\sum W}$$

Here the summation is over all stations, Z is the value at each station and W is the weighting function for that particular gridpoint and station.

This analysis uses four successive passes of the Cressman scheme. The program will not allow the Radius of Influence to be decreased so far that any gridpoint is out of range of all stations. If this occurs, the Cressman scheme is run again with the same radius of influence as

the last pass so that all fields will have the same amount of smoothing inherent in the analysis done to them. This did occur in some cases but never earlier in the process than the fourth pass. The decrease in the station residuals from successive passes was checked in all cases and found to be acceptable.

Kinematic Omega ω

ω is assumed to be 0 at the lowest level and is found by the equation in finite difference form

$$\omega_{ijl} = \omega_{ijl-1} + [(u_{i+1jl} - u_{i-1jl})/2\Delta x + (v_{ij+1l} - v_{ij-1l})/2\Delta x]\Delta P$$

and is integrated upwards from the lowest level.

ΔP in this case is defined as the depth of the representative layer as such

```
----------------------------- 200 mb

250 mb          4              ΔP=175 mb use div at 250 mb
----------------------------- 375 mb

500 mb          3              ΔP=225 mb use div at 500 mb


----------------------------- 600 mb

700 mb          2              ΔP=175 mb use div at 700 mb
----------------------------- 775 mb

850 mb          1              ΔP=225 mb use div at 850 mb


----------------------------- 1000 mb          ω = 0
```

Moisture

The moisture field is given as specific humidity q where

$$q = \frac{\text{mass of water vapor}}{\text{mass of dry air}}$$

also

$$q = \frac{r}{1+r}$$

where r= mixing ratio

$$r = \frac{\varepsilon\ e}{p-e}$$

where e = saturation vapor pressure in Pascals

ε = .622

p = pressure in Pascals

$e = e_0 \exp [L_v/R_v(1/T_0 - 1/T_d)]$ from Clausius-Clapyron

where e_0 = 610.78 Pascals

T_0 = 273.78 K

L_v = 2.5E+06 Joules/Kg

R_v = 461 Joules/K Kg

so

$$q = \frac{\varepsilon\ e}{p-e(1-\varepsilon)} \qquad \text{units of Kg/Kg}$$

Moisture calculations were not used in the results of this study, however, runs of the analysis were made using the virtual temperature instead of the observed temperature to check the effect that moisture might have on the results. No significant changes were noted.